POLYMER-INORGANIC HYBRID MATERIALS: FORMATION, PROCESSING, CHARACTERIZATION AND APPLICATIONS

A Dissertation

Presented to the Faculty of the Graduate School

of Cornell University

In Partial Fulfillment of the Requirements for the Degree of

Doctor of Philosophy

by

Hitesh Arora

February 2010

POLYMER-INORGANIC HYBRID MATERIALS: FORMATION, PROCESSING, CHARACTERIZATION AND APPLICATIONS

Hitesh Arora, Ph. D.

Cornell University 2010

Polymers are soft macromolecules that can be structured and designed according to the need. The properties of these materials, however, are often limited due to purely organic nature of these macromolecules. Addition of an inorganic material into the polymer, however, results in a hybrid material with improved properties that are a combination of its constituents. In this dissertation, formation, processing, characterization and applications of two different polymer-inorganic hybrid systems are discussed, where order and dynamics of the hybrid material is driven by the polymer thermodynamics. The first system combines the block copolymer self-assembly with functional inorganic nanoparticles to generate nanostructured and nanoporous thin films. The order in the nanoporous thin films is determined by quantitative image analysis. Nanoporous films are used as templates to generate epitaxial and heteroepitaxial single crystalline nanostructures on silicon substrates. The single crystalline nanostructures are characterized through various microscopy and diffraction techniques to determine the lateral order, crystal structure and orientation of the resulting nanostructures on the substrate. The second system combines a thermoresponsive polymer with charged clay nanoparticles to form hybrid hydrogels with improved mechanical properties. Additional porosity is induced into the gels for faster swelling kinetics. The resulting super-porous hybrid gels are used in a device that induces directed motion by inducing the volume phase transition locally and propagating the volume phase transitions through the length of the gel.

BIOGRAPHICAL SKETCH

Hitesh Arora was born to Mr. R. C. Arora and Mrs. Indu Arora. Hitesh grew up in Ghaziabad and Delhi in India. He finished primary, secondary and high school at various Dayanand Anglo Vedic Public Schools in and around Delhi. In the year 2000, Hitesh was admitted to the Chemical Engineering department at Indian Institute of Technology (IIT)-Bombay for Bachelors of Technology degree. His first research experience was summer research under Prof. Devang V. Khakhar at IIT-Bombay, after which he decided to pursue research as a career. He then, following the advice of his mentor Prof. A. K. Suresh, went on to do research in the summer of the year 2003 at the National Chemical Laboratory at Pune under Dr. Guruswamy Kumaraswamy. He thoroughly enjoyed the research experience at highly sophisticated laboratory. In the year 2004, he was admitted to the Chemical Engineering department at Cornell University and joined the group of Prof. Ulrich Wiesner to pursue PhD in Chemical Engineering with minor in Materials Sciences and Engineering.

To mom and dad

ACKNOWLEDGMENTS

First and foremost, I would like to thank my advisor, Prof. Ulrich Wiesner, whose guidance and support makes this dissertation possible. His sense for finding interesting new research directions and finding good in seemingly ordinary results is something I hope to emulate one day. He has been a great mentor. I would also like to thank Prof. Michael Thompson who has helped me transition into materials science from chemical engineering more smoothly. I would like to thank my collaborators: Dr. Phong Du, Dr. Lilit Yeghiazarian, Dr. John Gregoire, Dr. Jerome Hyun, Prof. Karen Kavangh, Prof. Claude Cohen, Dr. Marleen Kamperman, Rahul Malik, Zihui Li and Prof. David Muller. In the end I would like to thank the entire Wiesner group, Dr. Surbhi Mahajan, Dr. Phong Du, Dr. Scott Warren, Dr. Andrew Burns, Dr. Jinwoo Lee, Dr. Rene Kogler, Dr. Erik Herz, Dr. Chris Orilall, Morgan Stefik, Teeraporn Suteewong, Michelle Chavis, Hiroaki Sai, Zihui Li, Srikant Iyer, Kahyun Hur and Rachel Dorin, for their help, intellectual discussions and support throughout the last 5 years. I would like thank the facility managers at CCMR and NBTC, Mick Thomas, John Grazul, John Hunt, Paul Bishop, John Sinnott, Teresa Porri, and Brian Bowman.

In the end, I would like to acknowledge the effort put in by my parents for my accomplishments. Without their support, my achievements would be impossible. From early on, my father (Mr. R. C. Arora) and mother (Mrs. Indu Arora) would teach me while I was in primary school, and ensured that I get proper education by attending school (which, if things went according to my plan, I had absolutely no intention of attending) and study subjects that I hated (and found sound reasons for not studying) so that I am not left behind in my class. My brother (Mr. Neelesh Arora) has guided and advised me more than any other person that I have known. I followed his example for most part of my life. His support to pursue Ph.D. degree was the most valuable.

TABLE OF CONTENTS

LIST OF FIGURES

CHAPTER 1

INTRODUCTION

Polymer-inorganic hybrid materials combine the best of two worlds, the soft nature of organic molecules that makes the structured assembly possible and the functional nature of the inorganic materials. Studying such hybrids is interesting from a fundamental research point of view as well as for development of applications. The properties of the hybrid materials are a combination of the constituent organic and inorganic components and can be tuned by the choice of constituents and their relative fractions in the hybrid. Ideally, each component adds new properties, e.g. inorganic nanoparticles when added to a polymer enhance its mechanical, electrical, thermal or responsive properties while keeping the soft nature of the organic macromolecules which allow it to be molded or structured. Additionally, the self assembly of organic macromolecules can be used to structure direct the inorganic materials resulting in ordered nanostructured hybrids or on removal of the organics, to porous functional inorganic materials.

In this dissertation, I will discuss formation of functional nanocomposites, their processing, characterization and applications. Two different hybrid material systems will be discussed. The first system involves combining block copolymer self assembly with functional inorganic nanoparticles to generate nanostructured hybrid and porous surfaces.

The second system employs thermoresponsive polymer-clay nanoparticle hybrid hydrogels, with superior mechanical properties than the neat polymer hydrogels while retaining the thermoresponsive nature of the polymer component. The application of such hybrids to generate motility devices will be discussed.

Block copolymer derived nanostructured surfaces

Nanostructured surfaces combine material properties with structure at the nanometer length scale leading to higher surface area. Such materials provide a platform to perform fundamental studies to understand, e.g. the changes in material properties approaching very small scales and are quite useful for a variety of potential applications such as filtration, catalysis, plasmonics, or energy conversion and storage.

Lithography, deposition and etching processes are commonly used to generate nanostructured surfaces. Although very well understood and developed, these processes are fast approaching their fundamental limits. An alternative are self-assembly approaches which provide access to nanoscale features with greater ease and at less cost. Block copolymer self assembly[1], where two linked polymer chains phase separate spontaneously at length scales of typically 5-50 nm, is a promising approach to generate functional nanostructured materials for the future[2].

Block copolymers are a class of polymers where two distinct polymer chains are covalently bonded. These chains when incompatible with each other phase separate at length scales comparable to the size of the chains (~ tens of nanometers)[1] forming a wide variety of tunable phases. The morphology of the block copolymer melt is governed by the interaction between the two blocks as well as the size of the chains. The free energy of interaction between distinct polymer chains is determined by the Flory-Huggins equation[3]:

$$\frac{\Delta G_m}{k_B T} = \frac{\phi_A}{N_A} \ln \phi_A + \frac{\phi_B}{N_B} \ln(\phi_B) + \phi_A . \phi_B \chi$$

where $\emptyset_A$ and $\emptyset_B$ are the volume fractions of polymer chains A and B, N_A and N_B are the degree of polymerization of each polymer and χ is the monomer-monomer interaction parameter between the monomers of A and B. The first two terms

determine the entropic and the last term the enthalpic contribution to the free energy change when two polymer chains interact. Block segregation is favored due to their non-favorable enthalpic interactions counterbalanced by the loss in entropy due to localization of the interface between the blocks and chain stretching to maintain uniform density. Different phases have been predicted[4, 5] and experimentally[6] shown to exist for diblock copolymers of different volume fractions and thermodynamic parameters (χN), see the theoretical morphology diagram in Fig. 1.1. For a given block copolymer system, the volume fraction of the blocks determine the equilibrium morphology of the melt. The block chemistry could, however, be used to selectively swell one block of the copolymer with inorganic nanoparticles or precursors causing a phase formation different than the neat copolymer.

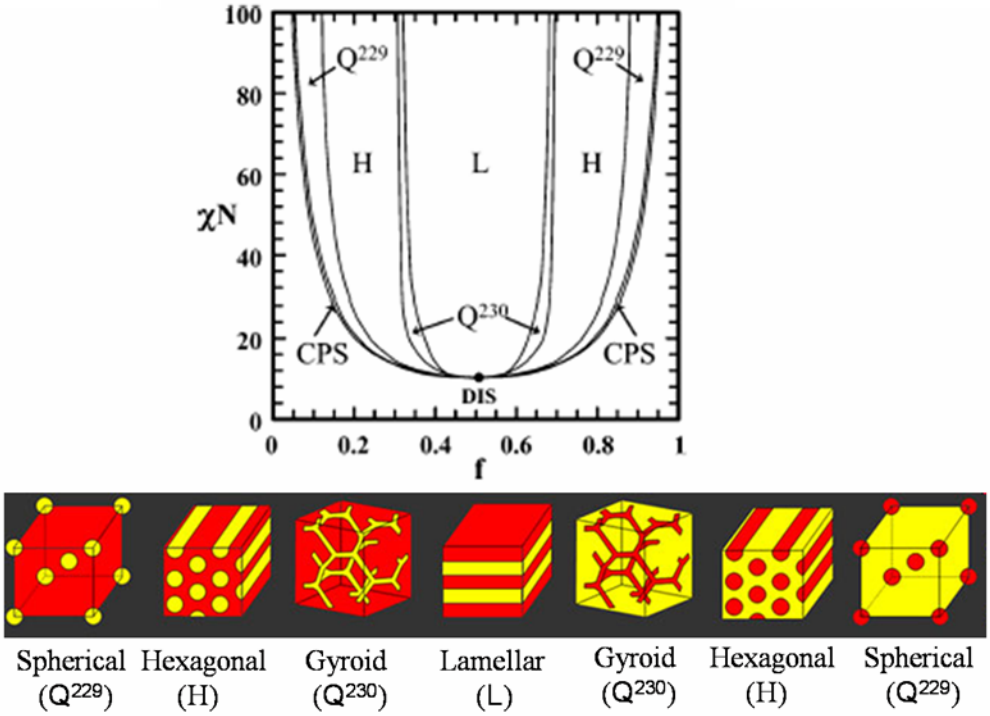

Figure 1.1: Diblock copolymer morphology diagram[5].

In this way, the entire morphology diagram could be mapped out by simply varying the inorganic content to change the effective volume fractions of the two domains[7], see Fig. 1.2. The selective swelling is driven by the favorable enthalpic interaction between the polymer and additives (nanoparticles or molecular precursors). This selective swelling of a block not only changes the effective volume fraction of the block but also changes the effective interaction parameter between the blocks. For strong interactions (such as hydrogen bonding) between the inorganic nanoparticles and one block, the monomer-nanoparticle interaction parameter is negative[8]. Addition of nanoparticles is advantageous as their properties can be tuned separately before adding them to the block copolymer solutions to obtain hybrids of desired properties.

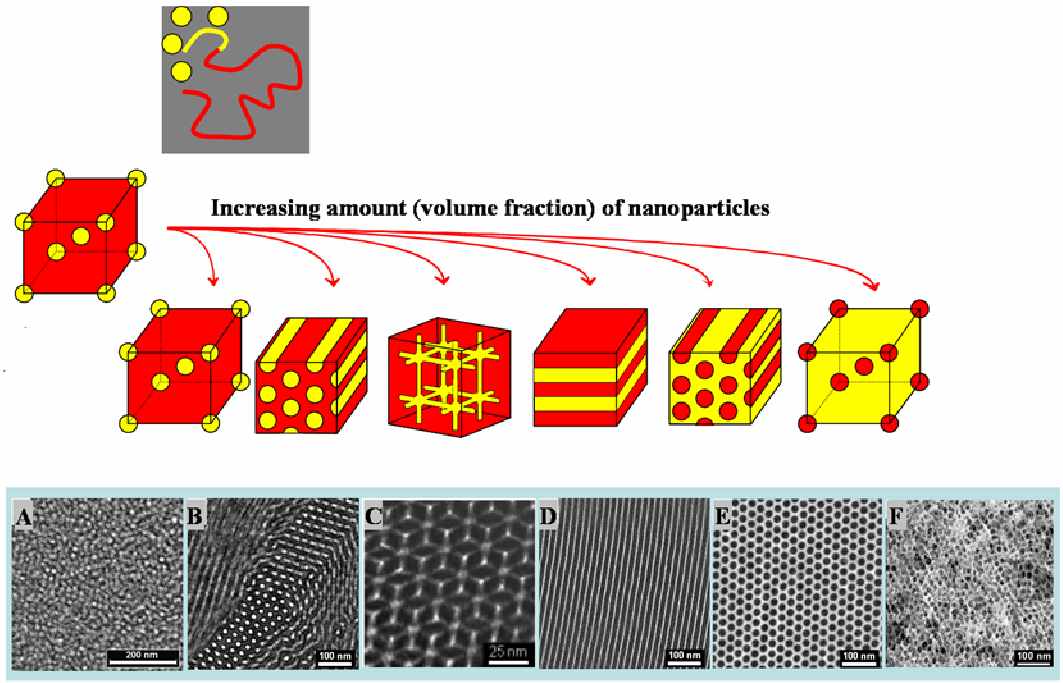

Figure 1.2: Schematic showing morphologies obtained on addition of nanoparticles to a block copolymer. (A-F) TEM images of the morphologies obtained upon increasing the amount of aluminosilicate nanoparticles to PI-*b*-PEO[7].

In the bulk, extensive research has been performed to structure direct silicates[9], aluminoslicates[7], transition metal oxides[10, 11], high temperature non-oxides[12] and metals[13, 14] using block copolymers. In contrast, in thin films, fewer studies have been reported on block copolymer derived hybrid formation. In general, most studies have focused on low loadings of nanoparticles into the desired block, resulting in low nanoparticle densities. This is mainly due to often limited solubility of the inorganic nanoparticles in organic solvents and/or the lack of strong enthalpic polymer-nanoparticle interactions. Furthermore, it often remains a challenge to synthesize uniform sized nanoparticles smaller than the block length of the polymer to prevent entropy driven segregation of nanoparticles[15, 16].

In this dissertation, I will present results on generating nanostructured thin films using block copolymer self-assembly with nanoparticles on surfaces. Assembly of three different block copolymer systems, (PI-*b*-PEO, PI-*b*-PDMAEMA and PS-*b*-PDMAEMA) with two types of inorganic nanoparticles (sol-gel derived aluminosilicate and ligand stabilized platinum nanoparticles) in thin films will be discussed along with their processing and characterization. Finally, applications of these nanostructured surfaces towards generating single crystal nanostructured arrays as well as single crystal over layers will be discussed.

Thermoresponsive-clay nanocomposites based motility device

Transformation of energy into directed motion requires different forms of complexity at different length scales. Nature demonstrates several mechanisms for inducing motion, at different length scales, through various organisms. It is desirable to mimic these natural systems to make efficient devices for MEMS and microfluidics. The devices based on biological systems have demonstrated that directed motion can be induced using e.g. adenosine triphosphate (ATP) powered biomolecules such as

motor proteins[17-19]. However, the stringent physiological conditions required and complexity involved in integration with the synthetic components of the device often limits the applicability of such systems. In contrast, a responsive synthetic material, that can endure more severe conditions, may provide the necessary robustness and more freedom to tune parameters as per the requirement. Synthetic materials such as polymer hydrogels that respond to changes in the environment such as pH[20, 21], temperature[22, 23], electric field[24] and light[25] are ideal for such devices. The responsive nature of these hydrogels has been exploited to make devices useful for applications ranging from biotechnology[26, 27] to microfluidics[28, 29].

Polymer gels are highly crosslinked networks of polymer chains which can hold large amounts of solvent in them. They can undergo volume phase transitions involving volume changes by releasing/uptaking solvent in their network, see fig. 1.3, induced by an external stimulus[30]. Volume phase transition is a process where the free energy is minimized through the balancing of three forces, generated by: rubber elasticity, polymer-polymer affinity, and ion pressure, collectively described as osmotic pressure[31], summarized in the following equation[3]:

$$\begin{aligned}\Delta F &= \Delta F_m + \Delta F_{el} + \Delta F_i \\ &= kT[n\ln(1-\varphi) + \chi n\varphi] + \frac{3\nu kT}{2}(\alpha^2 - 1 - \ln\alpha) - \nu fkT\ln\varphi\end{aligned}$$

where ΔF_m is the mixing energy of the polymer network with solvent, ΔF_{el} the elastic energy, and ΔF_i the energy due to counter ions for ionic gels; n is the number of solvent molecules in the gel, $\varphi=\varphi_0 (V_0/V)$ the volume fraction of the polymer network, V_0 the gel volume as synthesized, V is the gel volume, φ_0 the volume fraction of the polymer network as synthesized, χ the polymer-solvent interaction parameter, ν the total number of chains in the gel, $\alpha = (V/V_0)^{1/3}$ the linear swelling ratio, k the

Boltzmann constant, T the absolute temperature, and f the number of counter ions per chain

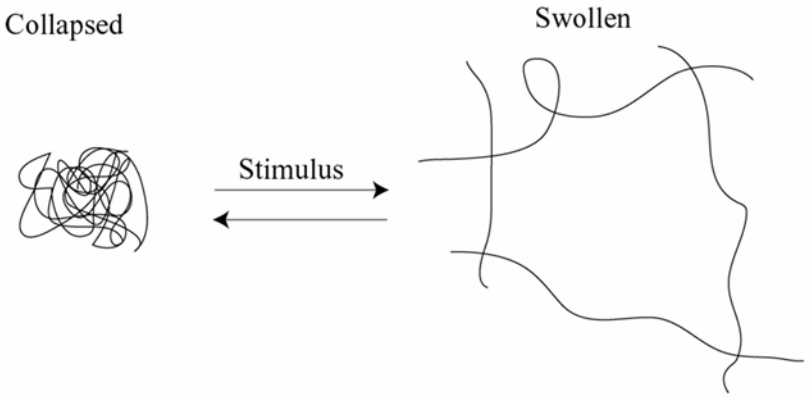

Figure 1.3: Schematic showing transition between the collapsed and swollen state of a responsive polymer gel on applying stimulus.

The ratio of swelling/shrinking is determined by factors such as fraction of ions on the backbone and crosslinking density. These factors also determine whether the transition is discontinuous or continuous[21]. The hydrolysis time to ionize the chains is typically several days and is often the limiting step for applications where large volume changes are required. The mechanical properties of such purely organic materials are also quite limited with pure gels often breaking apart upon applying stress. Incorporating clay nanoparticles, however, significantly enhances the mechanical properties of the hybrid hydrogels. Additionally, the charges on the nanoparticle surface alleviate the need for additional hydrolysis required to induce large volume changes upon inducing phase transitions.

In this dissertation, I will demonstrate a motility device based on thermoresponsive hybrid hyrogels that induces directed motion by breaking the symmetry of the volume

phase transitions of the hydrogel. The mechanism of motion is similar to that shown by an earthworm.

Outline of the dissertation

The dissertation is divided into 6 chapters:

Chapter 2 discusses generation of nanostructured platinum (Pt) thin films using block copolymer self assembly combined with ligand stabilized Pt nanoparticles. The films were characterized using AFM and SEM to elucidate the structure of the films. The conductance of the film was measured to determine the interconnectivity of the Pt nanoparticles.

Chapter 3 deals with generating block copolymer self assembly derived porous aluminosilicate thin films. The surface structure of the films was characterized by AFM and quantitative analysis of the order of the phase separated structure was performed using easy to read voronoi diagrams. The films were then used as templates to generate single crystal nanostructured nanopillar arrays through pulse laser irradiation and melt induced flow.

Chapter 4 extends the approach from chapter 3 to grow nickel silicide heteroepitaxially on silicon where the pores generated through block copolymer self assembly provide necessary confinement to grow heteroepitaxial films with lattice mismatch.

Chapter 5 deals with making a novel motility device using volume phase transitions of organic-inorganic hybrid gels. The motion is induced by breaking the symmetry of the phase transitions and propagating the thermal stimuli across the gel length.

Chapter 6 presents conclusions of the dissertation and discusses the future directions.

REFERENCES

1. Bates, F. S., Polymer-Polymer Phase Behavior. *Science* **1991,** 251, (4996), 898-905.

2. Bates, F. S.; Fredrickson, G. H., Block Copolymer--Designer Soft Materials. *Physics Today* **1999,** 52, 32-38.

3. Flory, P., *Principles of Polymer Chemistry*. Cornell University Press: Ithaca, NY, 1953.

4. Matsen, M. W.; Bates, F. S., Unifying Weak- and Strong-Segregation Block Copolymer Theories. *Macromolecules* **1996,** 29, (4), 1091-1098.

5. Cochran, E. W.; Garcia-Cervera, C. J.; Fredrickson, G. H., Stability of the Gyroid Phase in Diblock Copolymers at Strong Segregation. *Macromolecules* **2006,** 39, (7), 2449-2451.

6. Hamley, I. W., *The physics of block copolymers*. Oxford University Press: New York, 1998.

7. Templin, M.; Franck, A.; Du Chesne, A.; Leist, H.; Zhang, Y.; Ulrich, R.; Schadler, V.; Wiesner, U., Organically Modified Aluminosilicate Mesostructures from Block Copolymer Phases. *Science* **1997,** 278, (5344), 1795-1798.

8. Simon, P. F. W.; Ulrich, R.; Spiess, H. W.; Wiesner, U., Block Copolymer-Ceramic Hybrid Materials from Organically Modified Ceramic Precursors. In 2001; Vol. 13, pp 3464-3486.

9. Zhao, D. Y.; Feng, J. L.; Huo, Q. S.; Melosh, N.; Fredrickson, G. H.; Chmelka, B. F.; Stucky, G. D., Triblock copolymer syntheses of mesoporous silica with periodic 50 to 300 angstrom pores. *Science* **1998,** 279, (5350), 548-552.

10. Yang, P. D.; Zhao, D. Y.; Margolese, D. I.; Chmelka, B. F.; Stucky, G. D., Generalized syntheses of large-pore mesoporous metal oxides with semicrystalline frameworks. *Nature* **1998,** 396, (6707), 152-155.

11. Lee, J.; Orilall, M. C.; Warren, S. C.; Kamperman, M.; Disalvo, F. J.; Wiesner, U., Direct access to thermally stable and highly crystalline mesoporous transition-metal oxides with uniform pores. *Nature Materials* **2008,** 7, (3), 222-228.

12. Kamperman, M.; Garcia, C. B. W.; Du, P.; Ow, H. S.; Wiesner, U., Ordered mesoporous ceramics stable up to 1500 degrees C from diblock copolymer mesophases. *Journal of the American Chemical Society* **2004,** 126, (45), 14708-14709.

13. Warren, S. C.; Messina, L. C.; Slaughter, L. S.; Kamperman, M.; Zhou, Q.; Gruner, S. M.; DiSalvo, F. J.; Wiesner, U., Ordered Mesoporous Materials from Metal Nanoparticle-Block Copolymer Self-Assembly. *Science* **2008,** 320, (5884), 1748-1752.

14. Warren, S. C.; Wiesner, U., Self-assembled ordered mesoporous metals. *Pure and Applied Chemistry* **2009,** 81, (1), 73-84.

15. Thompson, R. B.; Ginzburg, V. V.; Matsen, M. W.; Balazs, A. C., Predicting the mesophases of copolymer-nanoparticle composites. *Science* **2001,** 292, (5526), 2469-2472.

16. Warren, S. C.; DiSalvo, F. J.; Wiesner, U., Nanoparticle-tuned assembly and disassembly of mesostructured silica hybrids. *Nat Mater* **2007,** 6, (2), 156-161.

17. Vale, R. D.; Reese, T. S.; Sheetz, M. P., Identification of a novel force-generating protein, kinesin, involved in microtubule-based motility. *Cell* **1985,** 42, (1), 39-50.

18. Schnitzer, M. J.; Block, S. M., Kinesin hydrolyses one ATP per 8-nm step. *Nature* **1997,** 388, (6640), 386.

19. van den Heuvel, M. G. L.; de Graaff, M. P.; Dekker, C., Molecular Sorting by Electrical Steering of Microtubules in Kinesin-Coated Channels. *Science* **2006,** 312, (5775), 910-914.

20. Ludk Toman, M. J., Jií Spváek, Jií Brus, Antonín Sikora, Jií Horský, Petr Vlek, Petra Látalová, Amphiphilic conetworks. IV. Poly(methacrylic acid)-l-polyisobutylene and poly(acrylic acid)-l-polyisobutylene based hydrogels prepared by two-step polymer procedure. New pH responsive conetworks. *Journal of Polymer Science Part A: Polymer Chemistry* **2009,** 47, (5), 1284-1291.

21. Tanaka, T.; Fillmore, D.; Sun, S.-T.; Nishio, I.; Swislow, G.; Shah, A., Phase Transitions in Ionic Gels. *Physical Review Letters* **1980,** 45, (20), 1636.

22. Xiao-Ding Xu, C.-S. C., Zong-Chun Wang, Gan-Rui Wang, Si-Xue Cheng, Xian-Zheng Zhang, Ren-Xi Zhuo, Click chemistry for in situ formation of thermoresponsive P(NIPAAm-co-HEMA)-based hydrogels. *Journal of Polymer Science Part A: Polymer Chemistry* **2008,** 46, (15), 5263-5277.

23. Hirokawa, Y.; Tanaka, T., Volume phase transition in a nonionic gel. *The Journal of Chemical Physics* **1984,** 81, (12), 6379-6380.

24. Tanaka, T.; Nishio, I.; Sun, S.-T.; Ueno-Nishio, S., Collapse of Gels in an Electric Field. *Science* **1982,** 218, (4571), 467-469.

25. Suzuki, A.; Tanaka, T., Phase transition in polymer gels induced by visible light. *Nature* **1990,** 346, (6282), 345-347.

26. Yu, L.; Ding, J., Injectable hydrogels as unique biomedical materials. *Chemical Society Reviews* **2008,** 37, (8), 1473-1481.

27. Peppas, N. A.; Hilt, J. Z.; Khademhosseini, A.; Langer, R., Hydrogels in Biology and Medicine: From Molecular Principles to Bionanotechnology. *Advanced Material* **2006,** 18, (11), 1345-1360.

28. Beebe, D. J.; Moore, J. S.; Bauer, J. M.; Yu, Q.; Liu, R. H.; Devadoss, C.; Jo, B.-H., Functional hydrogel structures for autonomous flow control inside microfluidic channels. *Nature* **2000,** 404, (6778), 588-590.

29. Liu, R. H.; Qing, Y.; Beebe, D. J., Fabrication and characterization of hydrogel-based microvalves. *Journal of Microelectromechanical Systems* **2002,** 11, (1), 45-53.

30. Li, Y.; Tanaka, T., Phase Transitions of Gels. *Annual Review of Materials Science* **1992,** 22, 243-277.

31. Tanaka, T., Gels. *Scientific American* **1981,** 244, (1), 124-138.

CHAPTER 2

"ONE-POT" BLOCK COPOLYMER DERIVED NANOPOROUS PLATINUM THIN FILMS[2]

Abstract

Porous metal films have high potential for use in applications such as catalysis, electrical contacts, plasmonics, and energy storage as well as energy conversion. Structuring metal thin films on the nanoscale to generate high surface areas poses an interesting challenge as metals have high surface energy. In this communication, we demonstrate formation of nanostructured metal thin films through spin coating of a mixture of block copolymers and ligand stabilized platinum nanoparticles. Plasma cleaning to remove the organics results in a conductive nanoporous platinum thin film. We expect that the method described here can be generalized to other metals and mixtures of metal nanoparticles.

[2] Hitesh Arora, Zihui Li, Marleen Kamperman, Ulrich Wiesner, *to be submitted*

Introduction

Block copolymer thin films are well studied for different block chemistries, sizes, and morphologies[1]. Their properties remain limited, however, due to the purely organic nature of these macromolecules, with a few exceptions[2]. In order to take advantage of block copolymers to structure inorganic functional materials at the nanoscale the block chemistry can be used to form e.g. metal rich domains[3-5] or one block can be removed selectively while the remaining block acts as a mask or template to structure inorganic materials[6-10]. In the bulk, "one-pot"-type approaches have been developed where block copolymers are mixed with inorganic nanoparticles or precursors to obtain high inorganic loadings. This concept has been successfully applied to generate nanostructured hybrid bulk films of silicates and aluminosilicates[11, 12], high temperature non-oxides[13], transition metal oxides[14] and metals[15-17]. Block copolymer hybrid formation has also been applied to thin films[18-21]. Most studies, however, have focused on low loadings of nanoparticles into the desired block, resulting in low nanoparticle densities. This is mainly due to often limited solubility of the inorganic nanoparticles in organic solvents and/or the lack of strong enthalpic polymer-nanoparticle interactions. Furthermore, it often remains challenging to synthesize uniform sized nanoparticles smaller than the block length of the polymer to prevent entropy driven segregation of nanoparticles[22, 23].

Here we report, on nanostructured metal thin films obtained through spin coating of solutions with high loadings of ligand stabilized metal nanoparticles (1-3 nm), structure directed by amphiphilic block copolymers. We demonstrate that after polymer removal, through appropriate plasma cleaning, metal nanoparticles form interconnected nanoporous networks as supported by electrical conductivity measurements.

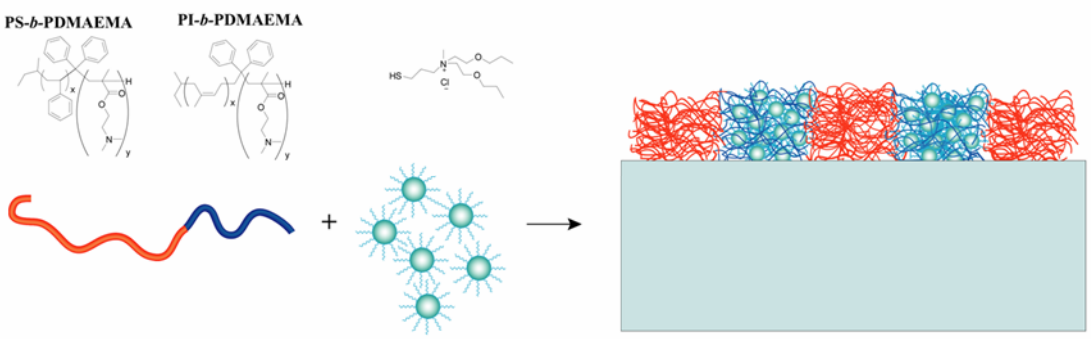

Figure 2.1: Schematic showing block copolymer and ligand chemistry.

Experimental section

Materials and processing

Figure 2.1 shows the block copolymers and ligand chemistry used in this work. The block copolymer and ligand stabilized nanoparticle synthesis has been described elsewhere[15]. In order to make films with high loadings of metal nanoparticles, block copolymer poly(isoprene-*b*-dimethylamino ethyl methacrylate) (PI-*b*-PDMAEMA, 31,000 g/mol; 33 % wt. PDMAEMA, polydispersity index = 1.05) was mixed with ligand stabilized platinum nanoparticles in a weight ratio of 1:3.14 (polymer:nanoparticles) in a solvent mixture of chloroform and methanol (9:1 wt./wt.). Solution concentrations of 0.8 wt. % and 1 wt. % [(polymer + nanoparticles)/solvent] were used to make films of 10-15 nm and 30 nm thickness, respectively. For films with low loadings of metal nanoparticles, poly(styrene-b- dimethylamino ethyl methacrylate) (PS-*b*-PDMAEMA, 34,200 g/mol; 14.6 % wt. PDMAEMA, polydispersity index = 1.08) was used with metal nanoparticles in a weight ratio of 1:0.40 (polymer:nanoparticles) in chloroform. A solution concentration of 1 wt. % [(polymer + nanoparticles)/solvent] was employed to make these films. The solutions were spin coated on piranha cleaned silicon wafers at 3000 rpm for 60 sec at an acceleration of 3000 rpms under ambient conditions.

Characterization

Atomic Force Microscopy: Atomic Force Microscopy (AFM) images were captured on a Veeco Nanoscope III in tapping mode with TappingMode. Etched Si probes (resonance frequency = 325 kHz, force constant = 37 N/m, tip radius of curvature = 10 nm; all values nominal) were used under ambient conditions.

Scanning Electron Microscopy: A Keck Field Emission SEM was used with an In-lens detector at 5 KeV to image the as-made and plasma cleaned films.

Conductance measurements: The resistance measurements were performed on the as-made and plasma cleaned samples using a I-V probe station with tungsten probes spaced 1 mm apart in Cornell Nanoscale Facility (CNF).

Results and discussion

High nanoparticle loadings

Figures 2.2a,b show AFM and SEM images of ~ 30 nm thick as-spun films from solutions of PI-b-PDMAEMA and ligand stabilized Pt nanoparticles. The images clearly reveal a phase separated nanostructure. The bulk morphology of samples of similar compositions was found to have a hexagonal lattice (data not shown). The AFM height image in Fig. 2.2a reveals the presence of both the organic and inorganic components with the majority component (the hydrophilic block plus platinum nanoparticles) preferentially wetting the surface, causing a height difference between the two domains. In the SEM image, in Fig. 2.2b, the platinum nanoparticle rich hydrophilic domains show up much brighter than the purely organic hydrophobic (PI) domains, confirming that the majority component is comprised of metal nanoparticles.

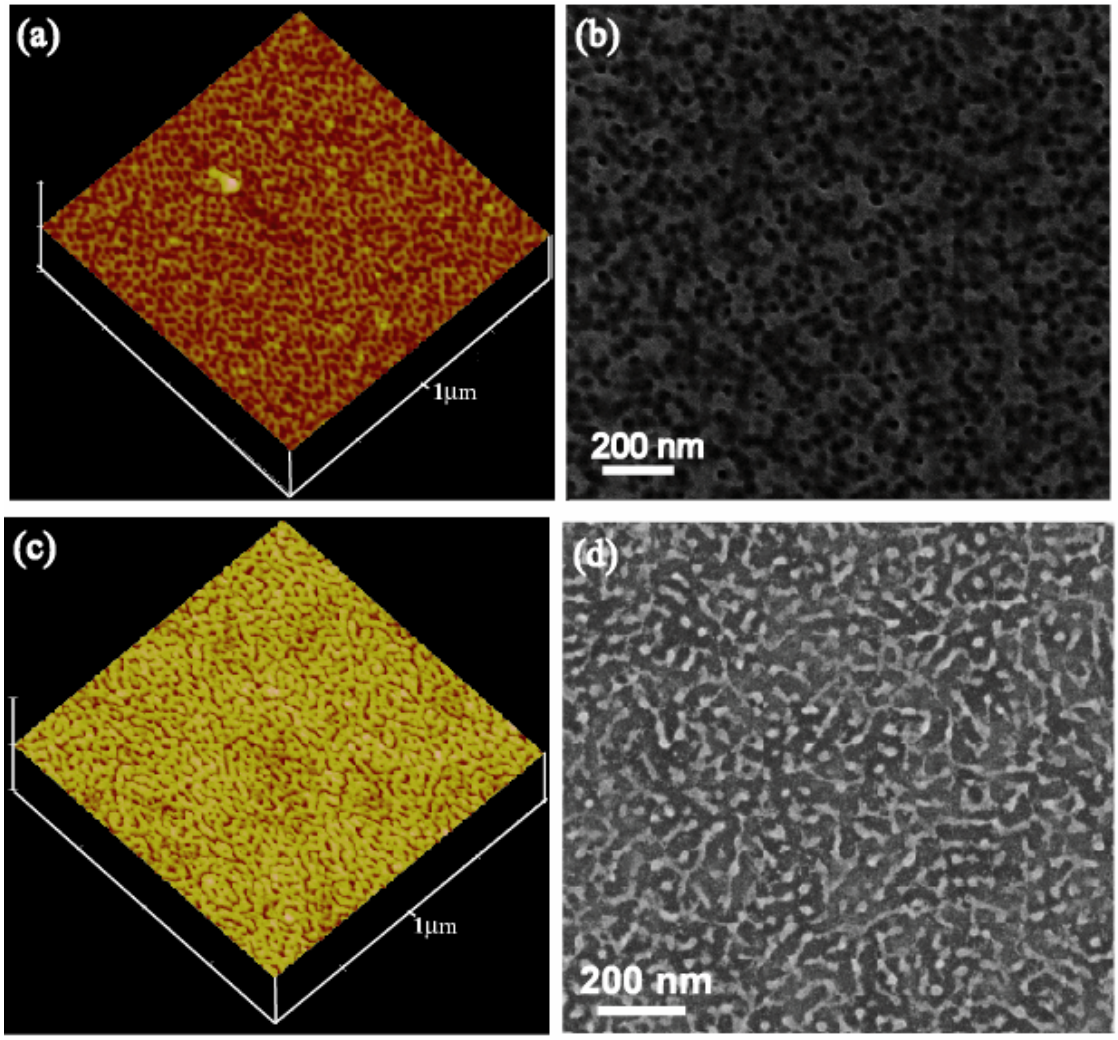

Figure 2.2: AFM height image of (a) as-made film with high loading of metal nanoparticles, (c) as-made film with low loading of metal nanoparticles. SEM image of (b) as-made film with high loading of metal nanoparticles, (d) plasma cleaned film with low loading of metal nanoparticles.

It is interesting to note that in the parent block copolymer the hydrophilic block PDMAEMA is the minority component (33 wt. %, see experimental section). Thus, by adding the ligand stabilized nanoparticles, from the present results the hydrophilic block is swollen selectively to convert into the majority component, consistent with earlier results in the bulk[15, 24].

As-made samples were further treated to remove the organics. First, the samples were heated to 450 °C under N_2 at a ramp rate of 5 °C/min and rapidly cooled to room temperature under N_2, followed by plasma cleaning to remove residual carbon. The resulting films displayed nanoporosity but also showed growth of large metal nanoparticles combined with an increase in wall thickness, see supporting information Fig. 2.S1. Therefore, in further experiments the as-made films were plasma cleaned only without any additional heat treatment. In this way the majority of the organics could be removed and the growth of nanoparticles was limited resulting in a neat nanoporous platinum film with the walls containing individual nanoparticles, see Fig. 2.3a,b.

From SEM images the pore spacing in as-spun samples varied between 39 and 43 nm. This is larger than the pore spacing of about 30 nm found in the corresponding equilibrated bulk samples (data not shown). The pore spacing in thin films further increased to ~54 nm when the film thickness was reduced to 10-15 nm through variations in the solution concentration, see experimental section. This suggests pinning of the film on the substrate limiting the lateral shrinkage of the film when the solvent evaporates, see supporting information Fig. 2.S2. The increase of pore spacing in thin films is expected as non-equilibrium morphologies are trapped through rapid solvent evaporation during spin coating.

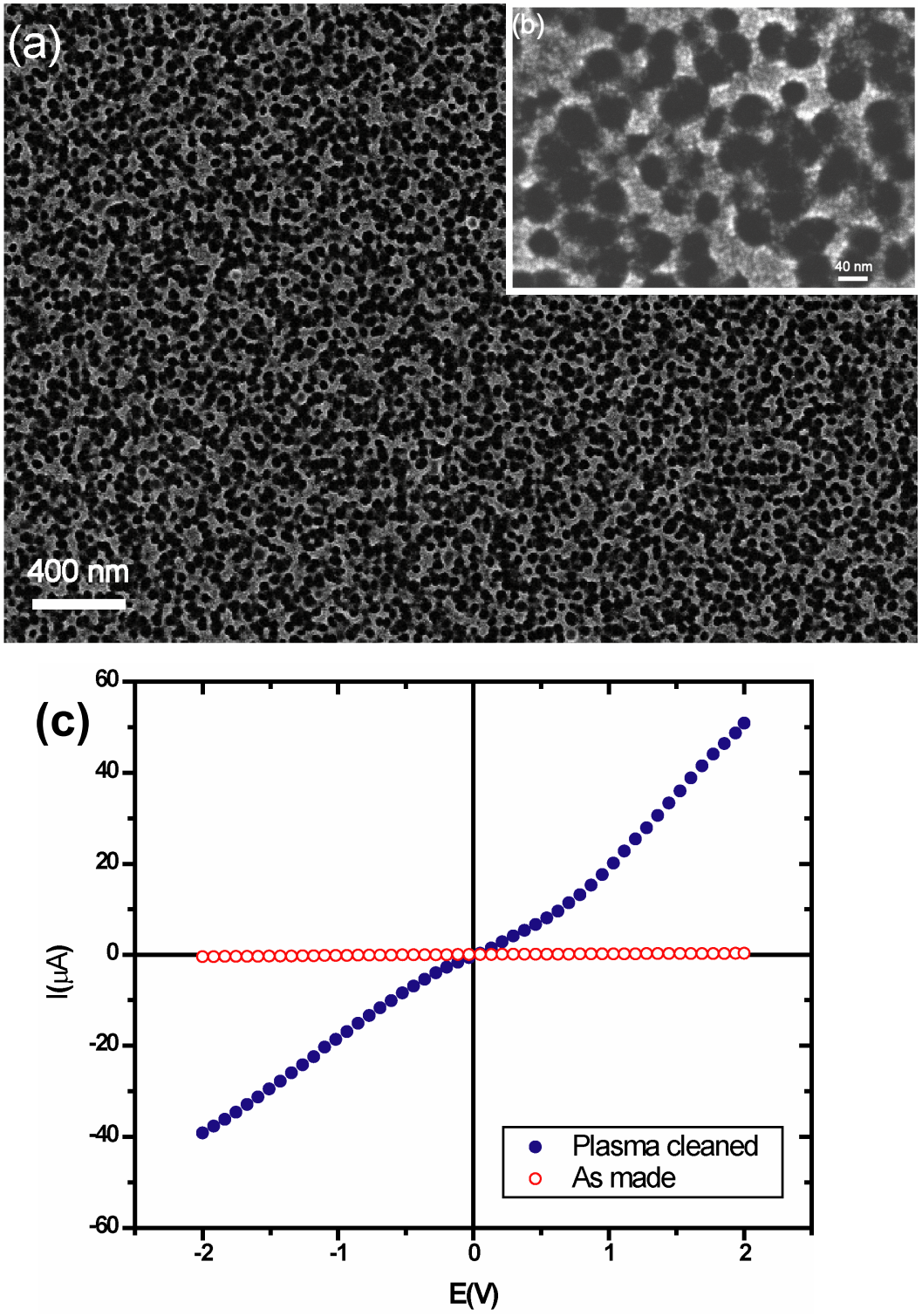

Figure 2.3: (a)-(b) SEM images of plasma cleaned thin films with high loadings of metal nanoparticles. (c) I-V curve of plasma cleaned film of high loading of metal nanoparticles.

Low nanoparticle loadings

Due to the low T_g (~ 215 K) of the PI block[25], thin films of PI-*b*-PDMAEMA with less metal nanoparticles and majority PI were mechanically unstable. Therefore, PS-*b*-PDMAEMA block copolymers containing a high T_g polystyrene block (T_g ~ 373 K)[26] were used for films with low loadings of metal nanoparticles. Thin films spin coated from dilute solutions of PS-*b*-PDMAEMA and ligand stabilized Pt nanoparticles showed worm-like/cylindrical morphologies. The AFM height image of an as-made sample, Fig. 2.2c, indicates that the PS block sticks out of the plane of the film. Upon plasma cleaning short worm-like structures are left behind, as revealed by SEM imaging, Fig. 2.2d. The characteristic spacing for these thin films (thickness ~ 30 nm) was found to vary between 40 and 45 nm as compared to a value of ~ 40 nm observed for bulk films (data not shown).

Resistance measurements

In order to test whether plasma cleaning leads to conductive metal films, resistance measurements were performed on as-made and plasma cleaned films of PI-b-PDMAEMA with high loadings of metal nanoparticles using a two point probe (spaced apart 1 mm). The voltage across the films was varied while the current was measured. In as-made films very low currents (~ pA) were observed suggesting that the ligands and the block copolymers insulate the Pt nanoparticles form one another. In contrast, in the plasma cleaned films a voltage dependant current was detected, see Fig. 2.3c, indicating contact between Pt nanoparticles. From the inverse of the slope of the I-V curve in Fig. 2.3c, a resistance of 46.4 KΩ was derived. This value is higher than that of non-porous platinum films of similar thickness but is similar to the values observed for very thin (~2 nm) platinum films[27]. The higher resistance of our films is likely due to the high porosity and/or limited interconnectivity between the Pt

nanoparticles in the films, increasing the path length of the electron flow across the film. It could also in part be due to some residual organics left behind from the plasma cleaning step.

In summary, in this communication we report on the direct one-pot formation of nanoporous platinum thin films by combining block copolymers with high loadings of ligand stabilized metal nanoparticles and leading to continuous platinum films after removal of the organics. Different morphologies were obtained by changing the metal loadings into the hydrophilic blocks of two different amphiphilic block copolymers. Finally, the conductance of the films was measured demonstrating connectivity of the metal nanoparticles upon removal of the organics (polymers and ligands). We expect that the method can be generalized to other metals by e.g. synthesizing nanoparticles of different metals, alloys or even intermetallics. Such highly nanoporous and conductive metal thin films may find applications in areas like catalysis, plasmonics and sensing.

Acknowledgements

The authors acknowledge financial support of this research by NSF (DMR-0404195 and DMR- 0605856) through the NIRT program and by a subcontract with Cornell University, Department of Materials Science and Engineering, under Prime Agreement Award Number 06-G-031 from the Department of Homeland Security. The research made use of facilities of Cornell Center for Materials Research (CCMR) with funding from the Materials Research Science and Engineering Center program of NSF (cooperative agreement DMR-0520404), Cornell Nanobiotechnology Center (NBTC) supported in part by the STC Program of the National Science Foundation

under Agreement No. ECS-9876771 and Cornell Nanoscale Facility (CNF) supported by the National Science Foundation under Grant No. ECS-0335765.

APPENDIX A

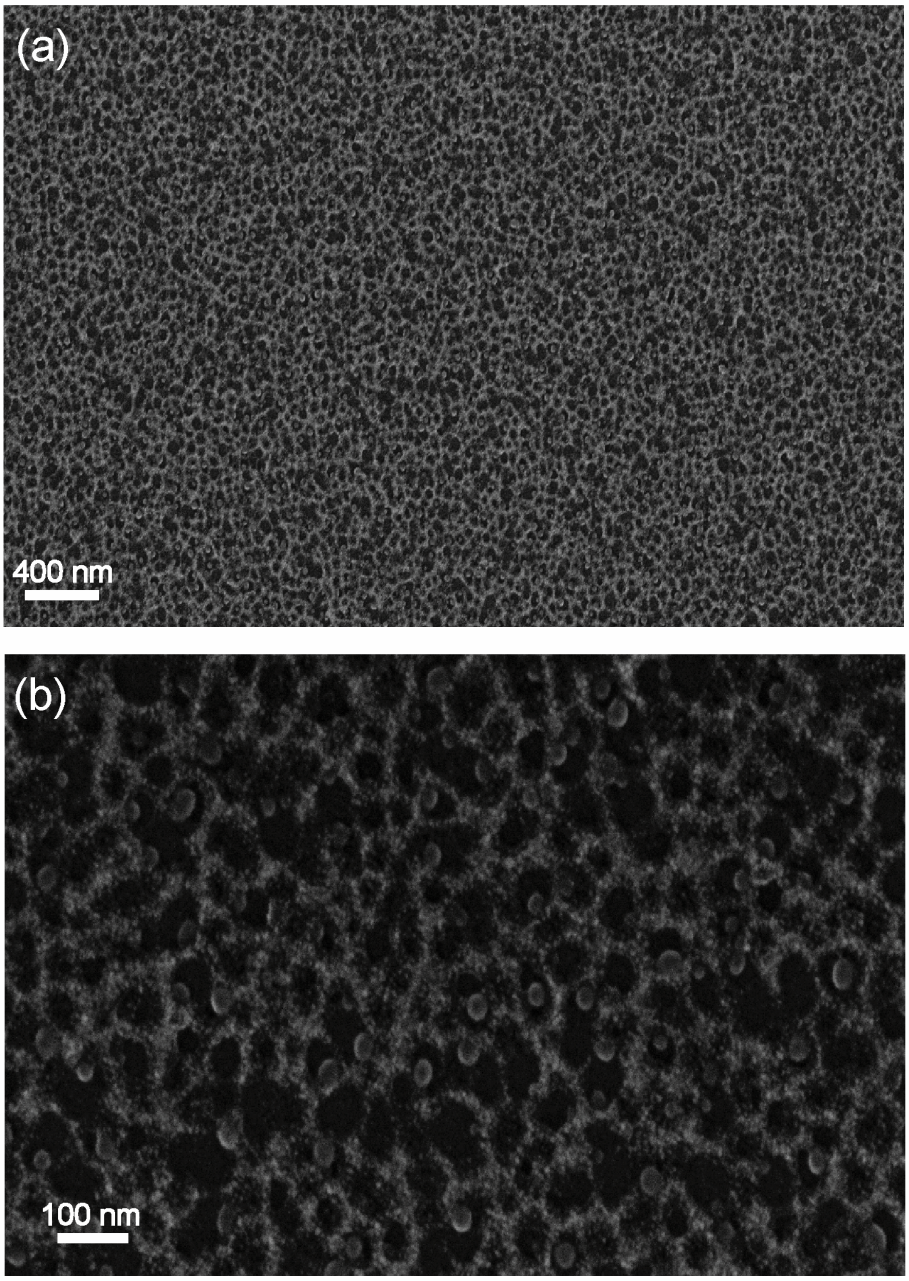

Figure 2.S1: (a)-(b) SEM images of pyrolysed thin films with high loadings of metal nanoparticles.

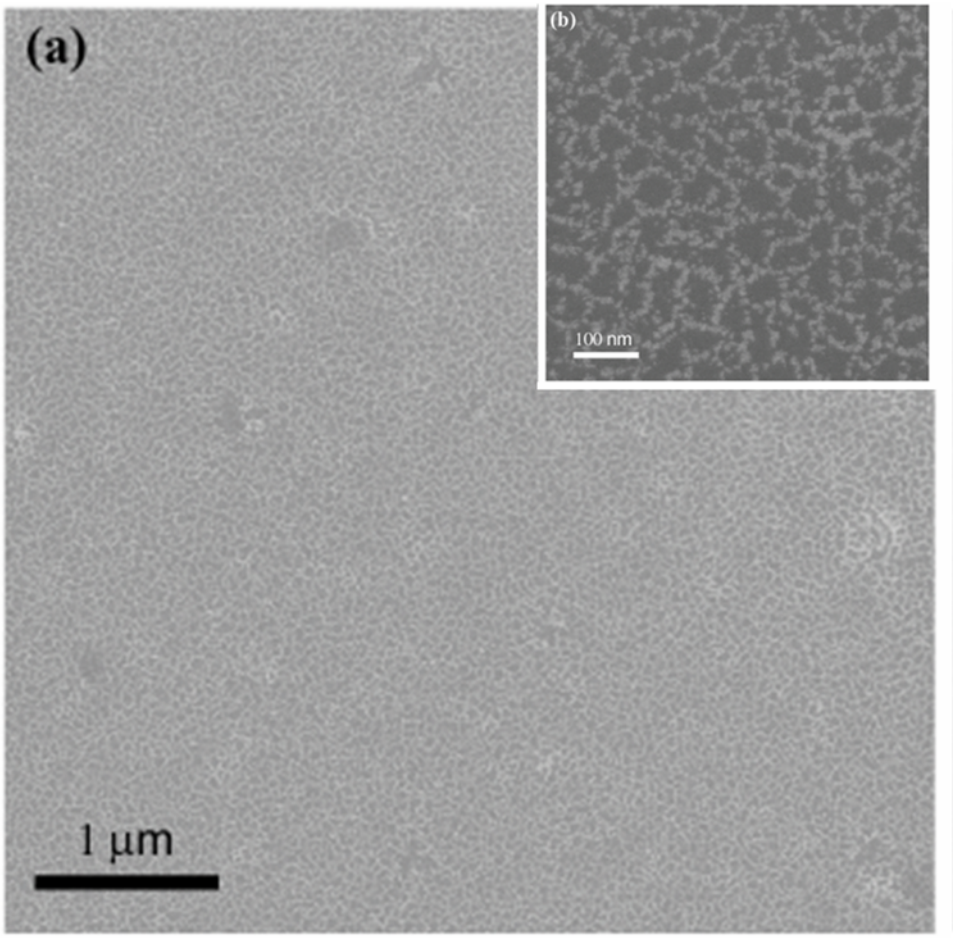

Figure 2.S2: SEM image of a plasma cleaned film with high loading of nanoparticles.

REFERENCES

1. Fasolka, M. J.; Mayes, A. M., Block Copolymer Thin Films: Physics and Applications[1]. *Annual Review of Materials Research* **2001,** 31, (1), 323.

2. Temple, K.; Kulbaba, K.; Power-Billard, K. N.; Manners, I.; Leach, K. A.; Xu, T.; Russell, T. P.; Hawker, C. J., Spontaneous Vertical Ordering and Pyrolytic Formation of Nanoscopic Ceramic Patterns from Poly(styrene-*b*-ferrocenylsilane). In 2003; Vol. 15, pp 297-300.

3. Lopes, W. A.; Jaeger, H. M., Hierarchical self-assembly of metal nanostructures on diblock copolymer scaffolds. *Nature* **2001,** 414, (6865), 735-738.

4. Gorzolnik, B.; Mela, P.; Moeller, M., Nano-structured micropatterns by combination of block copolymer self-assembly and UV photolithography. *Nanotechnology* **2006,** 17, (19), 5027-5032.

5. Chai, J.; Wang, D.; Fan, X.; Buriak, J. M., Assembly of aligned linear metallic patterns on silicon. *Nature Nanotechnology* **2007,** 2, (8), 500-506.

6. Hamley, I. W., Nanostructure fabrication using block copolymers. *Nanotechnology* **2003,** 14, (10), R39-R54.

7. Park, M.; Harrison, C.; Chaikin, P. M.; Register, R. A.; Adamson, D. H., Block Copolymer Lithography: Periodic Arrays of ~10^{11} Holes in 1 Square Centimeter. *Science* **1997,** 276, (5317), 1401-1404.

8. Crossland, E. J. W.; Kamperman, M.; Nedelcu, M.; Ducati, C.; Wiesner, U.; Smilgies, D. M.; Toombes, G. E. S.; Hillmyer, M. A.; Ludwigs, S.; Steiner, U.; Snaith, H. J., A Bicontinuous Double Gyroid Hybrid Solar Cell. *Nano Letters* **2008**.

9. Urade, V. N.; Wei, T.-C.; Tate, M. P.; Kowalski, J. D.; Hillhouse, H. W., Nanofabrication of Double-Gyroid Thin Films. *Chemistry of Materials* **2007,** 19, (4), 768-777.

10. Bhanu, N.; Gowd, E. B.; Nadja, C. B.; Alexander, E.; Petr, F.; Paul, S.; Manfred, S., Arrays of Inorganic Nanodots and Nanowires Using Nanotemplates Based on Switchable Block Copolymer Supramolecular Assemblies. *Advanced Functional Materials* **2009,** ASAP.

11. Templin, M.; Franck, A.; Du Chesne, A.; Leist, H.; Zhang, Y.; Ulrich, R.; Schadler, V.; Wiesner, U., Organically Modified Aluminosilicate Mesostructures from Block Copolymer Phases. *Science* **1997,** 278, (5344), 1795-1798.

12. Zhao, D.; Feng, J.; Huo, Q.; Melosh, N.; Fredrickson, G. H.; Chmelka, B. F.; Stucky, G. D., Triblock Copolymer Syntheses of Mesoporous Silica with Periodic 50 to 300 Angstrom Pores. *Science* **1998,** 279, (5350), 548-552.

13. Kamperman, M.; Garcia, C. B. W.; Du, P.; Ow, H. S.; Wiesner, U., Ordered mesoporous ceramics stable up to 1500 degrees C from diblock copolymer mesophases. *Journal of the American Chemical Society* **2004,** 126, (45), 14708-14709.

14. Yang, P.; Zhao, D.; Margolese, D. I.; Chmelka, B. F.; Stucky, G. D., Generalized syntheses of large-pore mesoporous metal oxides with semicrystalline frameworks. *Nature* **1998,** 396, (6707), 152-155.

15. Warren, S. C.; Messina, L. C.; Slaughter, L. S.; Kamperman, M.; Zhou, Q.; Gruner, S. M.; DiSalvo, F. J.; Wiesner, U., Ordered Mesoporous Materials from Metal Nanoparticle-Block Copolymer Self-Assembly. *Science* **2008,** 320, (5884), 1748-1752.

16. Warren, S. C.; Wiesner, U., Self-assembled ordered mesoporous metals. *Pure and Applied Chemistry* **2009,** 81, (1), 73-84.

17. Yusuke, Y.; Atsushi, S.; Ryoichi, M.; Azusa, T.; Kazuyuki, K., Mesoporous Platinum with Giant Mesocages Templated from Lyotropic Liquid Crystals Consisting of Diblock Copolymers13. *Angewandte Chemie* **2008,** 47, (29), 5371-5373.

18. Lin, Y.; Boker, A.; He, J.; Sill, K.; Xiang, H.; Abetz, C.; Li, X.; Wang, J.; Emrick, T.; Long, S.; Wang, Q.; Balazs, A.; Russell, T. P., Self-directed self-assembly of nanoparticle/copolymer mixtures. *Nature* **2005,** 434, (7029), 55-59.

19. Balazs, A. C.; Emrick, T.; Russell, T. P., Nanoparticle Polymer Composites: Where Two Small Worlds Meet. *Science* **2006,** 314, (5802), 1107-1110.

20. Kang, H.; Detcheverry, F. A.; Mangham, A. N.; Stoykovich, M. P.; Daoulas, K. C.; Hamers, R. J.; Muller, M.; de Pablo, J. J.; Nealey, P. F., Hierarchical Assembly of Nanoparticle Superstructures from Block Copolymer-Nanoparticle Composites. *Physical Review Letters* **2008,** 100, (14), 148303-4.

21. Oren, R.; Liang, Z.; Barnard, J. S.; Warren, S. C.; Wiesner, U.; Huck, W. T. S., Organization of Nanoparticles in Polymer Brushes. *Journal of the American Chemical Society* **2009,** 131, (5), 1670-1671.

22. Warren, S. C.; DiSalvo, F. J.; Wiesner, U., Nanoparticle-tuned assembly and disassembly of mesostructured silica hybrids. *Nat Mater* **2007,** 6, (2), 156-161.

23. Thompson, R. B.; Ginzburg, V. V.; Matsen, M. W.; Balazs, A. C., Predicting the mesophases of copolymer-nanoparticle composites. *Science* **2001,** 292, (5526), 2469-2472.

24. Jain, A.; Wiesner, U., Silica-type mesostructures from block copolymer phases: Formation mechanism and generalization to the dense nanoparticle regime. *Macromolecules* **2004,** 37, (15), 5665-5670.

25. Brandrup, J. I., Edmund H.; Grulke, Eric A.; Abe, Akihiro; Bloch, Daniel R., *Polymer Handbook (4th Edition).* John Wiley & Sons.: p pp: 208.

26. Brandrup, J. I., Edmund H.; Grulke, Eric A.; Abe, Akihiro; Bloch, Daniel R, *Polymer Handbook (4th Edition).* John Wiley & Sons: p 211-212.

27. Agustsson, J. S.; Arnalds, U. B.; Ingason, A. S.; Gylfason, K. B.; Johnsen, K.; Olafsson, S.; Gudmundsson, J. T., Electrical resistivity and morphology of ultra thin Pt films grown by dc magnetron sputtering on SiO2. *Journal of Physics: Conference Series* **2008,** 100, (8), 082006.

CHAPTER 3

EPITAXIAL AND HETEROEPITAXIAL NANOSTRUCTURES ON SINGLE CRYSTAL SUBSTRATES FROM BLOCK COPOLYMER SELF-ASSEMBLY AND LASER INDUCED MELT FLOW[2]

Abstract

One of the key challenges in the field of nanostructured inorganic solids is the development of single crystal materials. We present results on the formation of nanostructured single crystals from porous aluminosilicate thin films on single crystal silicon substrates obtained in a self-assembly process with block copolymers as structure directing agents. When irradiated with an excimer laser beam, the resulting molten silicon fills the pores and solidifies epitaxially from the substrate. Removal of the template leaves the single crystal nanostructures behind. Furthermore, the template allows confined heteroepitaxy of crystals with lattice mismatch. Deposition of a stoichiometric mixture of amorphous material and irradiation allows growing nanostructured nickel silicide heteroepitaxy on single crystal substrates, not possible with standard lithographic and etching techniques. Irradiation through a mask provides access to hierarchically structured single crystal materials. The results suggest a general strategy towards mesostructured single crystal materials for a wide variety of applications including energy generation and storage.

[2] Hitesh Arora, Phong Du, Jerome Hyun, David Muller, Michael Thompson, Ulrich Wiesner. *To be submitted.*

Introduction

Since the first report from researchers at Mobil in 1992 of inorganic materials whose structure could be directed by self-assembled organic molecules the field of mesostructured inorganic solids has attracted considerable research interest[1]. Moving from small molecular weight surfactants to blocked macromolecular architectures as structure directing agents[2] has connected the fields of inorganic chemistry and polymer science and has led to the development of materials as diverse as mesoporous silica[3], mesoporous transition metal oxides[4], mesoporous carbon[5], and mesoporous metals[6].

All of these materials prepared by so-called bottom-up synthesis strategies are either amorphous or polycrystalline. One of the key remaining issues in the field is the development of single crystal mesostructured inorganic materials. Such materials may enable considerable advances in areas like energy generation and storage. For example, the charge carrier mobility in small dimensions is significantly reduced by grain boundaries which decreases charge collection efficiency in photovoltaic cells[7]. While large area patterned inorganic single crystals have been synthesized before, the patterns have been limited to the micron-scale[8]. Block copolymer thin films have been used as etching mask to generate inorganic nanostructures but the features can only be vertically aligned and are always open from the top[9]. Laser-induced melting of silicon and subsequent infiltration into a quartz mold has been previously described[10]. The process relied on so-called top-down lithography and etching to make a mold, however, with structural period of hundreds of nanometers. Moreover, the epitaxial relation of the resulting structures to the substrate was not described and crystallization upon cooling could seed at the mask surface resulting in a polycrystalline nanostructure. Additionally, generation of nanosructures requires applying pressure to imprint the mold into the substrate as it is being melted by a laser

pulse. This requires mask of good mechanical strength which could be a limiting step when scaling down the size of nanostructures and mask to several 10's of nm. Directional rapid solidification and epitaxy have been described for semicrystalline block copolymer films but without any inorganic materials[11]. Hierarchically ordered oxide structures have been demonstrated before but the oxides were not single crystal materials[12].

In this work we used ordered mesoporous aluminosilicate thin films on Si to define and limit crystallization of Si with templates having periodicities on the tens of nanometer scale. Thin films were obtained in a bottom-up self-assembly approach using inorganic precursors structure directed by block copolymers. By excimer laser irradiation the template pores were filled with molten Si, which subsequently crystallized epitaxially from the substrate. Removal of the template led to single crystal nanostructures. Finally, laser irradiation through a mask provided access to hierarchically structured single crystal materials.

The process we used is schematically shown in Fig. 3.1a-g. Bare Si wafers were spun coat with a mixture of prehydrolyzed metal alkoxides [(3-glycidyloxypropyl-) trimethoxysilane and aluminum sec-butoxide, 8:2] and poly(isoprene-*b*-ethylene oxide) (PI-*b*-PEO) block copolymer in organic solvents (THF:Chloroform, 1:1). Monolayers with inverse hexagonal mesostructure were formed[13], with one inorganic-rich domain (PEO + inorganic) and the other purely organic (PI). The organic components were subsequently removed by slow heating to 500°C, leaving an ordered mesoporous hexagonal array, with pores accessible from the top, Fig. 3.1a. For the block copolymers employed here, the nanopore lattice spacings were between 30 and 35 nm depending on the polymer molecular weight. The physical film thickness after calcination was close to 15 nm, as determined by a combination of scanning electron microscopy and X-ray diffraction (data not shown). The mesopores were filled with Si

through use of 40 ns XeCl excimer pulsed laser irradiation (λ = 308 nm), Fig. 3.1h. The template itself is transparent with the laser light absorbed by the Si substrate. Time resolved reflectance (TRR) of the sample surface was monitored with a HeNe probe laser (λ = 650 nm) and was used to measure melt duration. At fluences (σ) above the melt threshold (~600 mJ/cm^2), the semiconducting solid becomes a metallic liquid and the surface reflectance increases sharply[14], Fig. 3.4a-d, providing a fingerprint for understanding the details of the process.

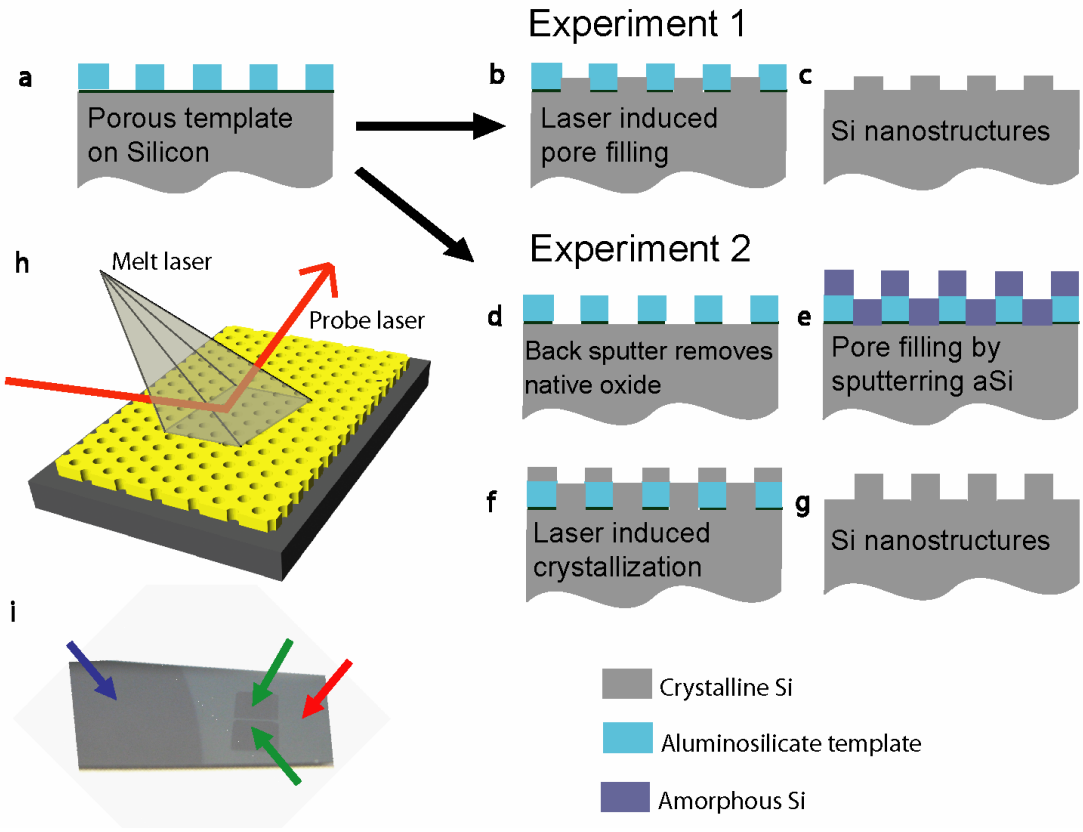

Figure 3.1 Schematic of single crystal Si nanostructure generation. (a) Porous template; (b)-(c) Experiment 1; (d)-(g) Experiment 2; (h) Laser annealing schematic. (i) Photograph of crystalline Si substrate with amorphous Si deposited (red arrow), spots after laser induced crystallization (green arrow) and bare crystalline Si (blue arrow).

In first experiments, sample I, the porous template was irradiated with the excimer laser at fluences sufficient to melt the underlying Si substrate. Because of rapid cooling into the substrate, the total melt-duration is limited to ~20-100 ns and the total time at higher temperatures is less than a few microseconds, preventing sintering collapse of the porous silica-type template. After laser irradiation, the aluminosilicate template was dissolved away using a 48 % HF solution to expose the resulting Si nanostructure, Figs. 3.1b and c. Auger spectroscopic measurements confirm no residual oxides with the remaining structures being pure Si (data not shown). Figs. 3.2a and b show AFM images of sample I before and after irradiation with five 40 ns duration laser pulses and subsequent removal of the skeletal aluminosilicate. The AFM results suggest excellent pattern transfer from the template into Si. The images were quantitatively analyzed using analysis tools described elsewhere[15 16]. Figs. 3.2f and g show representative Voronoi diagrams of the aluminosilicate template and the resulting nanostructured Si array, respectively. The Voronoi diagram represents the number of nearest neighbors of a pore or resulting Si nanostructure after melting and is color-coded to facilitate identification of defects and grain boundaries[16]. The Voronoi-6 ratio, defined as the fraction of pores or resulting Si nanostructures with 6-fold hexagonal nearest neighbor symmetry, provides a simple metric for sample comparison. As indicated by the increased number of defects in the Voronoi diagram, the transformation from pores to Si nanostructures increases disorder in the system. However, transfer of the template into Si structures is accomplished with a high yield, with greater than 90 % conversion of pores to Si nanostructures and only a 20 % decrease in the Voronoi-6 ratio, see Fig. 3.2k-sample I.

Figure 3.2 AFM images with respective height profiles. (a) and (c) porous templates; (b), (d) and (e) Si nanostructures. (f)-(j) Voronoi analysis of corresponding AFM images. (k) Table for sample I, II, III. RDF of (l) sample I, III and (m) sample II. Scan size for all AFM images is 1 μm and height scale bar is 30 nm. Scan area for Voronoi analysis is 2x2 μm^2.

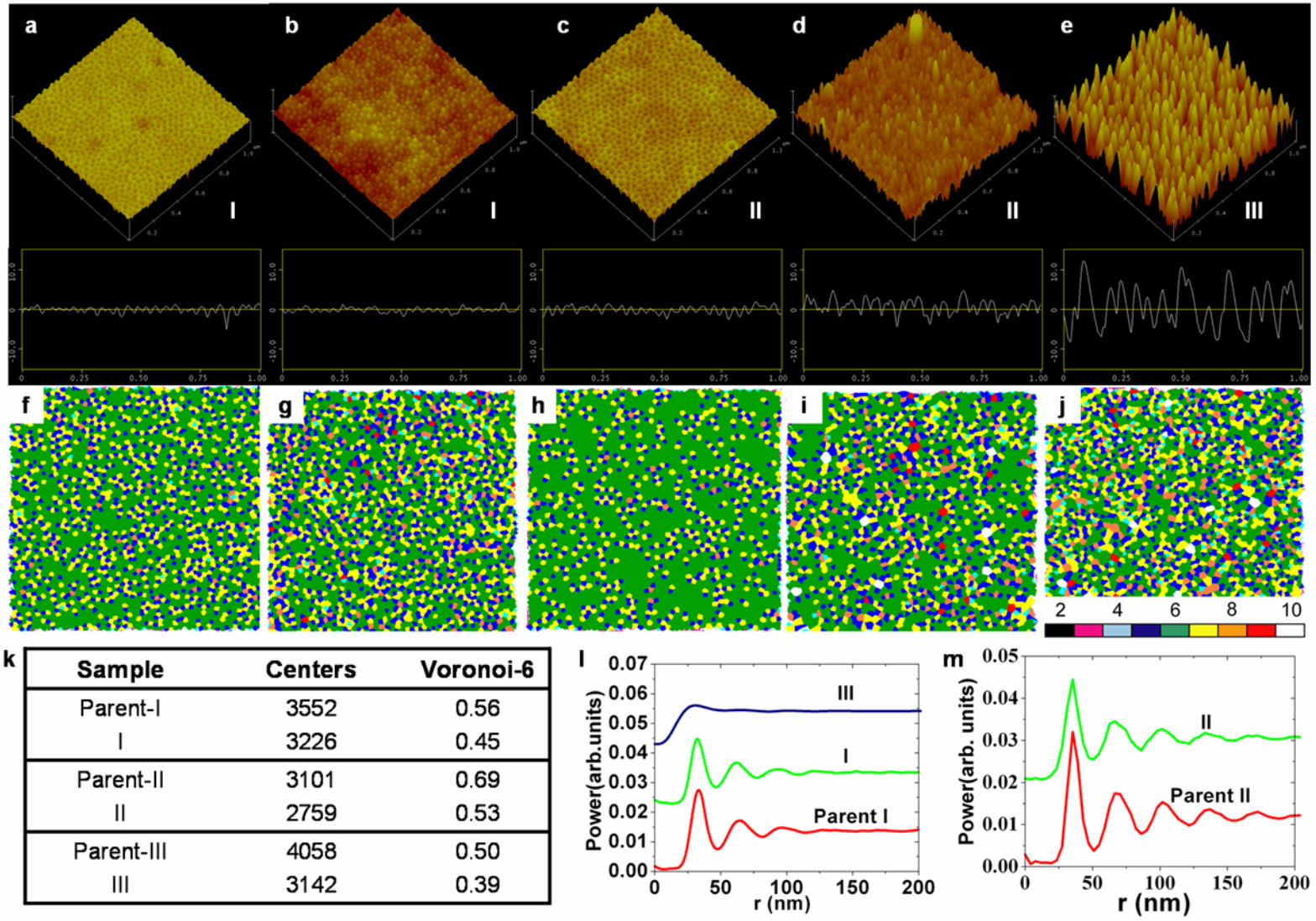

k

Sample	Centers	Voronoi-6
Parent-I	3552	0.56
I	3226	0.45
Parent-II	3101	0.69
II	2759	0.53
Parent-III	4058	0.50
III	3142	0.39

Although in these experiments the transfer fidelity was high in the lateral dimensions, section analysis of AFM images showed the resulting Si nanostructures to be only 1-2 nm high, see height profile in Fig. 3.2b. This motivated the development of a modified process in subsequent experiments enabling better filling of the pores thus forming taller Si nanostructures. To this end an amorphous Si (a-Si) overlayer, Fig. 3.1d-g, was deposited onto the template prior to laser annealing. Furthermore, the native oxide present at the bottom of the pore was first removed using Argon ions before sputter depositing a-Si in the same chamber and at the same base pressure. This creates direct contact between deposited a-Si in the pore and the crystalline Si (c-Si) substrate, Fig. 3.1e. As we will show below, laser irradiation at an energy density above the melt threshold of c-Si of sample films (sample II) prepared in this way resulted in epitaxial crystallization of Si nanopillars from the substrate inside the pore, Fig. 3.1f. Subsequent HF (48 %) treatment removed the oxide template leaving behind an array of single crystal nanopillars, Fig. 3.1g. The AFM image and Voronoi analysis, Figs. 3.2c-d and h-i, respectively, of the template and pillar array confirmed 89 % pattern transfer and only 23 % decrease in the Voronoi-6 ratio, Fig. 3.2k-sample II. The average height of pillars was found to be 6-7 nm i.e. significantly higher than before, see height profile in Fig. 3.2d.

The epitaxial crystallinity of the Si nanopillars was confirmed by imaging pillar cross sections with High Resolution Transmission Electron Microscopy (HR-TEM) and Scanning TEM (STEM), Fig 3.3. The presence of lattice fringes in the pillars in congruence with the fringes in the substrate, Fig. 3.3a and b, clearly show the crystalline nature of the nanopillars. The epitaxial growth of the nanopillars was confirmed by STEM mode imaging where the Si substrate and nanopillar are both shown to be aligned along the [110] zone axis, Figs. 3.3c and d. A 2D Fast Fourier

Transform (FFT) pattern on the substrate and pillar, inset in Figs. 3.3c and d, show that the two areas share the [111] reflections. Due to an offset in depth that exceeds the 16 nm depth of focus of the microscope, STEM mode images were taken with only the pillar, Fig. 3.3c, and only the substrate, Fig. 3.3d, in focus. Electron Energy Loss Spectroscopy (EELS) on the pillars, inset in Fig 3.3c, revealed the presence of a crystalline Si-L edge peak at 100 eV, also seen in the spectrum of c-Si-sub, see inset in Fig. 3.3d. The small peak at 108 eV in the spectrum in Fig. 3.3c is the signature for Si in silicon oxide that may have grown when the sample surface was exposed to air after HF acid treatment.

In order to elucidate single crystal mesostructure formation mechanism, we performed a series of experiments (sample III) where the a-Si was deposited without etching the native oxide layer present at the bottom of the pore, thereby preventing direct contact between a-Si and c-Si substrate. The native oxide layer is expected to prevent molten Si from flowing through the pores. Deposited Si should thus remain confined to the pores (or on top of the template) when melted by the excimer laser pulse. This in turn should result in maximum height Si nanopillars (~15 nm). This was indeed observed, see AFM analysis Fig. 3.2e. Voronoi analysis of AFM data reveals a 77 % pore to pillar conversion with 22% decrease in the Voronoi-6 ratio, Figs. 3.2j and k-sample III.

Figure 3.3: (a) and (b) TEM images of nanostructure cross section. The apparent shift at the interface is not a physical stacking fault but rather a contrast reversal in the phase-contrast image when the projected thickness of the sample changes – the substrate is thicker than the pillar and the electrons undergo a larger phase shift in the substrate. STEM images which do not suffer from contrast reversals with thickness for (c) nanostructure in focus and (d) Si substrate in focus. (e) Cross-section STEM of NiSi-Si interface with corresponding EELS spectra. Corresponding EELS spectra and FFT inset in (c) and (d).

a
5 nm
b
1 nm
Ni L-Edge
Counts
E(eV)
c
5 nm
d
5 nm
e
1 nm
eV

For further quantitative data analysis, the radial distribution functions (RDF) of the AFM images were computed for the parent templates I and II as well as the resulting Si nanostructures/pillars, Figs. 3.2l and m. The RDFs of the unirradiated templates, Parent I-II, exhibit narrow first order maxima and multiple higher order peaks. For the case of no deposited a-Si, the RDF of the resulting Si surface nanostructure (sample I), shows very similar characteristics to the template with only slightly less power in each peak due to the slightly increased disorder. The same result was obtained for sample II. In contrast, sample III behaves quite differently. The RDF of this sample, i.e. of Si nanopillars formed from a template plus deposited a-Si with the native oxide still present, exhibits a first order maximum shifted to larger distances (r = 39 nm) as compared to the template (r = 31 nm) and a rapid decay without additional higher order peaks. When examining the AFM image in more detail at the local scale there were sequences of pillars with the expected nearest neighbor distance (i.e. r = 31 nm). However, they were surrounded by neighbors with distances closer to the expected second nearest neighbor value. This suggests that a significant number of pores simply did not get filled, consistent with the 37 % loss of centers from the Voronoi analysis. The corresponding RDF maximum indeed lies in-between the nearest and second nearest neighbor radii and may be caused by a slight deformation of the template toward the empty space upon Si melting.

Figure 3.4 (a) Time Resolved Reflectance signal on (I) bare Si at $\sigma = 700$ mJ/cm^2, (II) bare Si at $\sigma = 800$ mJ/cm^2, and (III) sample I at $\sigma = 800$ mJ/cm^2. (b) Amorphous Si deposited on bare Si (I) first irradiation at $\sigma = 700$ mJ/cm^2, (II) second irradiation at $\sigma = 500$ mJ/cm^2 after (I), (III) second irradiation at $\sigma = 700$ mJ/cm^2 after (I).(c) Amorphous Si deposited on bare Si (I) first irradiation at $\sigma = 500$ mJ/cm^2, (II) second irradiation at $\sigma = 500$ mJ/cm^2 after (I). (d) Sample II (I) first irradiation at $\sigma = 700$ mJ/cm^2, (II) second irradiation at $\sigma = 700$ mJ/cm^2 after (I). Onsets of the TRR signal rise vary based on the time delay in data acquisition due to changes in the set up that occurred in between measurements. Optical micrograph (e) a copper TEM grid and (f) the resultant pattern on sample III (with deposited amorphous Si over the template) after laser exposure. (g) and (h) AFM images after HF treatment. Scan size is 2μm x 2μm and the I–bar along the z-axis is 40 nm in (h).

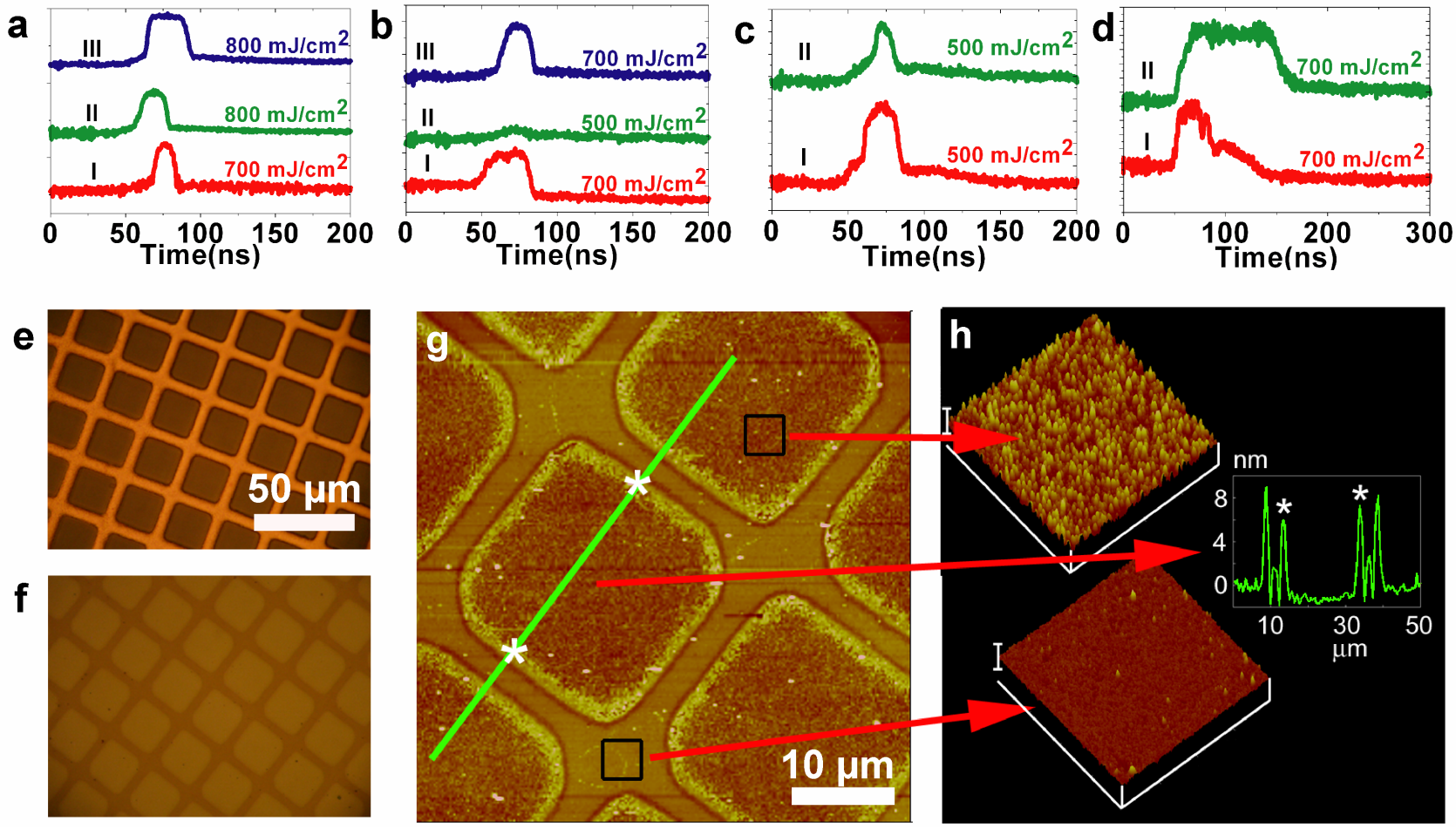
a
III
800 mJ/cm2
II
800 mJ/cm2
I
700 mJ/cm2
0 50 100 150 200
Time(ns)
b
III
700 mJ/cm2
II
500 mJ/cm2
I
700 mJ/cm2
0 50 100 150 200
Time(ns)
c
II
500 mJ/cm2
I
500 mJ/cm2
0 50 100 150 200
Time(ns)
d
II
700 mJ/cm2
I
700 mJ/cm2
0 100 200 300
Time(ns)
e
50 μm
f
g
10 μm
h
nm
8
4
0
10 30 50
μm

To obtain insight into the Si melt transient behavior during laser annealing, we monitored the time resolved reflectance (TRR) of samples with and without the template and a-Si coating. Irradiated above the melt threshold, the reflectance of a bare c-Si substrate will jump as the melt first forms, will remain constant while the melt front propagates into the substrate, and finally decreases abruptly as the surface solidifies, see Fig. 3.4a I. Small changes in the reflectance prior to melt result from simple surface heating[17]. We investigated three other scenarios: (a) the c-Si substrate with the porous template, (b) the c-Si substrate with a-Si on top, and (c) the c-Si substrate with template and a-Si deposited on top. With just the porous template (case a), the TRR signal remained very similar, though the melt duration increased by ~8 ns at σ = 800 mJ/cm^2 (Figs. 3.4a II and III). On the time scale of the laser pulse and melt duration, the crosslinked silica-type template is not expected to undergo any significant structural change. The extended melt duration arises partially from the anti-reflective nature of the porous template coating[18], but also suggests incorporation of a low concentration of impurities (possibly oxygen or aluminium) during solidification.

In case (b), with a-Si deposited directly on the c-Si substrate, the TRR signal strongly depends on the fluence. With a lower melting temperature, the melt threshold for a-Si is less than that of c-Si[19]. Epitaxial solidification can only occur for fluences sufficient to melt into the c-Si substrate (Fig. 3.4b I), with polycrystalline Si (poly-Si) resulting at lower fluences[20]. Transformation of the a-Si can be readily confirmed visually (Fig. 3.1i). After irradiation above 700 mJ/cm^2, samples behave similar to the bare substrate with melt threshold near 600 mJ/cm^2 (Figs 3.4b II-III). However, for initial irradiations below the melt threshold for c-Si, e.g. at 500 mJ/cm^2, a peak is observed in the TRR signal for case (b), Fig. 3.4c I. On irradiating the spot again at this fluence the peak remains (Fig. 3.4c II), suggesting the formation of poly-Si.

From these results we concluded that in order to epitaxially crystallize a-Si deposited in the template pores, case (c), sample had to be irradiated above the melt threshold of c-Si. Upon irradiation, Fig. 3.4d I, the reflectance first increased rapidly, then stayed constant followed by a steep first drop and finally further decreased gradually over several tens of nanoseconds. The drop in reflectance in two steps is likely due to the different time scales involved for heat transfer from molten Si to the substrate (i) within a pore (faster) and (ii) at the top of the template which is a poor heat conductor (slower). During a second irradiation at the same spot, Fig. 3.4d II, the reflectance signal exhibits a single peak and decay suggesting the absence of Si on top of the template. Because more a-Si was deposited than necessary to fill the pores we speculate that this could only happen if the deposited Si on top of the template flowed through the pores to move under the template displacing it upwards. The poor wetting properties[21] between molten Si and aluminosilicate template might propel this surface tension driven flow of molten Si through the template.

Interestingly, the pore sizes accessible through block copolymer self assembly can provide necessary confinement to grow heteroepitaxy on single crystal substrates for materials with moderate lattice mismatch. Here we demonstrate nickel silicide heteroepitaxy on c-Si-sub by sputter depositing amorphous stoichiometric NiSi (deposition rates were monitored using a crystal monitor and checked with XPS on the surface of the films) on the porous aluminosilicate templates, after removing any native oxide, and then crystallizing the silicide using the pulse laser melting of the silicide. The selective melting of the silicide minimizes the Ni diffusion or incorporation of Si from the substrate into the liquid phase, thus maintaining the correct stoichiometry in the pore. The epitaxial orientation of the strained NiSi lattice on c-Si-sub was confirmed by STEM images of the NiSi-Si interface, see Fig. 3.3e.

The EELS data collected on the pillar and the substrate clearly indicate presence of Ni-L-edge peak on the pillar and absence of Ni below the interface. These results clearly show efficacy of the process to generate NiSi heteroepitaxy within the confined pores of the template.

Finally, the present bottom-up fabrication of epitaxially grown inorganic mesostructures was combined with top-down lithographic approaches to define specific areas thus providing access to hierarchical single crystal nanostructures. As a proof-of-principle experiment, a TEM grid was used as a simple mask during the laser irradiation process to form patterns on a micron scale, Fig. 3.4e. The grid was placed in contact with the sample surface to minimize loss of fidelity from the divergence of the homogenized incident laser beam (see Fig. 3.S1 in the supporting information for the laser setup). The resulting Si pattern after irradiation through the TEM grid, Fig. 3.4f, indicates remarkable transfer. Template removal by HF and subsequent AFM imaging shows distinct squares of patterned material, Fig. 3.4g. Close-up images, Fig 3.4h, of the square confirm Si nanostructures in the irradiated area and smooth flat Si in areas under the mask. As the image in Fig. 3.4g suggests and the AFM cross section analysis confirms, Fig. 3.4h, the pattern edges of the irradiated areas are significantly higher than the interior of the areas. Despite poorly controlled edge effects, this simple proof-of-principle experiment does demonstrate, however, that the placement of single crystal nanostructures can be controlled through simple imaging methods. Arbitrarily complex shapes should thus be accessible by leveraging the wealth of patterning techniques currently available.

The results presented here give clear evidence that block copolymer directed inorganic mesopores can be transformed into single crystal mesostructures of various materials—currently demonstrated for Si and NiSi, but likely to be extensible to any

material with a reasonable melting temperature and liquid viscosity. Use of the polymer precursors offers tremendous variability in structural parameters, such as pore size, pore-to-pore correlation, pore wall thickness, etc. The symmetry of the phase is not restricted to hexagonal ordering since various structures are known to exist in the phase diagram of diblock copolymers, including simple cubic, lamellar, and cubic bicontinuous[22]. Furthermore, through masks an additional level of control on the micron length scale enables placement of these single crystal structures at predefined locations and in arbitrary shapes. This approach may open up a range of novel processing technologies for the generation of hierarchical ordered, mesoporous, single crystal materials. For example, extended 3D galleries may be accessible by repeated processing or flow into thicker films. Such galleries, etched of their silica skeletons, could enable formation of thick mesoporous and single crystal films for applications e.g. in energy generation and storage.

Acknowledgements

The authors acknowledge financial support of this research by NSF (DMR-0404195) through the NIRT program, use of facilities of the Cornell Center for Materials Research (CCMR) with funding from the Materials Research Science and Engineering Center program of NSF (cooperative agreement DMR-0520404), Cornell Nanoscale Facility (CNF) supported by the National Science Foundation under Grant No. ECS-0335765 and Cornell Nanobiotechnology Center (NBTC) supported in part by the STC Program of the National Science Foundation under Agreement No. ECS-9876771. The authors would also like to thank John Gregoire for help with a-Si sputter deposition, Andrew Burns for help with the schematic, Pinshane Huang for help with

collecting EELS data and Carlos Garcia and Scott Warren for providing block copolymers A and B, respectively.

APPENDIX B

Experimental section

Porous Template: Porous templates were prepared using two PI-*b*-PEO block copolymers A and B with molecular weights of 38,700 g/mol (32 wt.% PEO) and 27,300 g/mol (13.6 wt.% PEO), respectively, as described elsewhere [13]. Pore-pore spacing for monolayer type films from these polymers were ~31 nm (polymer A, samples I and III) and ~35 nm (polymer B, sample II).

Oxide removal and sputter deposition: Prior to sputter deposition on the templates, the native oxide was removed by *in-situ* back sputtering with argon ions at a base pressure of 2.3×10^{-7} torrs for 30 sec at removal rates of 9.55 nm/min. a-Si was sputtered in the same chamber and at the same base pressure for 85 sec at deposition rates of 12 nm/min. 12 nm of thermally evaporated a-Si was deposited on sample 3 under ultrahigh vacuum without removing the native oxide. Stoichiometric NiSi was sputter deposited at base pressure of 2.3×10^{-7} torrs for 55 sec at deposition rates of 18.6 nm/min.

Laser Annealing: A 40 ns pulse duration XeCl excimer (304 nm) laser was used to melt Si. Reflectance of the sample surface was monitored using a 650 nm HeNe laser. The laser irradiated area on the sample was 3.5x3.5 mm^2. Energy densities are referenced to a melt fluence of 600 mJ/cm^2 for bare single crystal Si wafers. Four irradiations at an energy density of 700 mJ/cm^2 were used to melt the Si in samples II and III. Sample I was irradiated five times at an energy density of 800 mJ/cm^2. The NiSi samples were annealed once at an energy density of 550 mJ/cm^2

Hydrofluoric Acid treatment: Samples were treated with 48 % HF acid for 1-2 minutes.

Characterization: Atomic Force Microscopy (AFM) images were captured on a Veeco Nanoscope III in tapping mode with TappingMode Etched Si probes (resonance frequency = 325 kHz, force constant = 37 N/m, tip radius of curvature = 10 nm; all values nominal) under ambient conditions. HRTEM and STEM were performed on a Tecnai F20 microscope at 200 keV.

TEM sample preparation : The TEM samples were prepared by a wedge-polishing and ion-milling method [23], whereby initially a bare Si piece was glued to the sample surface to prevent any damage that may occur to the pillars throughout the preparation process. The NiSi TEM sample was prepared using focussed ion beam. A protective carbon and platinum layer was deposited before milling the sample to protect the film from milling damage.

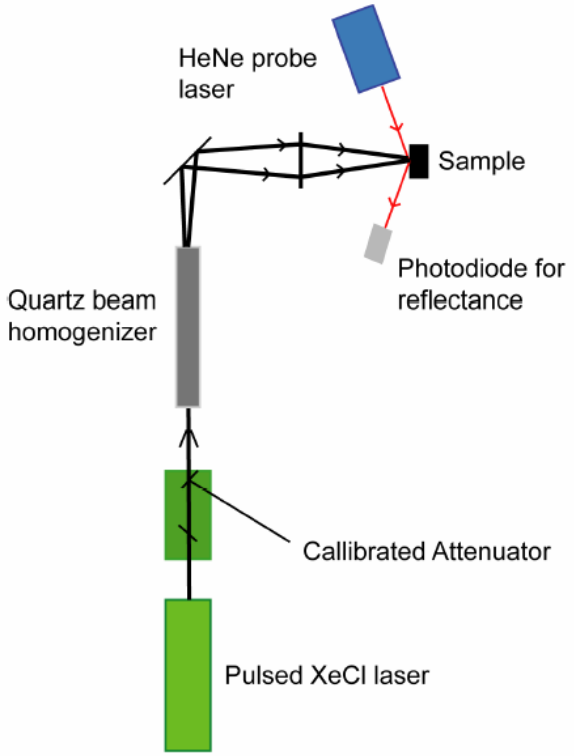

Figure 3.S1: Schematic of laser annealing setup

REFERENCES

1. Kresge, C. T.; Leonowicz, M. E.; Roth, W. J.; Vartuli, J. C.; Beck, J. S., Ordered mesoporous molecular sieves synthesized by a liquid-crystal template mechanism. *Nature* **1992,** 359, (6397), 710-712.

2. Templin, M.; Franck, A.; Du Chesne, A.; Leist, H.; Zhang, Y.; Ulrich, R.; Schadler, V.; Wiesner, U., Organically Modified Aluminosilicate Mesostructures from Block Copolymer Phases. *Science* **1997,** 278, (5344), 1795-1798.

3. Zhao, D.; Feng, J.; Huo, Q.; Melosh, N.; Fredrickson, G. H.; Chmelka, B. F.; Stucky, G. D., Triblock Copolymer Syntheses of Mesoporous Silica with Periodic 50 to 300 Angstrom Pores. *Science* **1998,** 279, (5350), 548-552.

4. Yang, P.; Zhao, D.; Margolese, D. I.; Chmelka, B. F.; Stucky, G. D., Generalized syntheses of large-pore mesoporous metal oxides with semicrystalline frameworks. *Nature* **1998,** 396, (6707), 152-155.

5. Joo, S. H.; Choi, S. J.; Oh, I.; Kwak, J.; Liu, Z.; Terasaki, O.; Ryoo, R., Ordered nanoporous arrays of carbon supporting high dispersions of platinum nanoparticles. *Nature* **2001,** 412, (6843), 169-172.

6. Warren, S. C.; Messina, L. C.; Slaughter, L. S.; Kamperman, M.; Zhou, Q.; Gruner, S. M.; DiSalvo, F. J.; Wiesner, U., Ordered Mesoporous Materials from Metal Nanoparticle–Block Copolymer Self-Assembly. *Science* **2008,** 320, (5884), 1748-1752.

7. Vere, A. W., *Crystal Growth: Principles and Progress*. Springer: 1988; p 276.

8. Aizenberg, J.; Muller, D. A.; Grazul, J. L.; Hamann, D. R., Direct Fabrication of Large Micropatterned Single Crystals. *Science* **2003,** 299, (5610), 1205-1208.

9. Park, M.; Harrison, C.; Chaikin, P. M.; Register, R. A.; Adamson, D. H., Block Copolymer Lithography: Periodic Arrays of ~10^{11} Holes in 1 Square Centimeter. *Science* **1997,** 276, (5317), 1401-1404.

10. Chou, S. Y.; Keimel, C.; Jian, G., Ultrafast and direct imprint of nanostructures in silicon. *Nature* **2002,** 417, (6891), 835.

11. De Rosa, C.; Park, C.; Thomas, E. L.; Lotz, B., Microdomain patterns from directional eutectic solidification and epitaxy. *Nature* **2000,** 405, (6785), 433-437.

12. Yang, P.; Deng, T.; Zhao, D.; Feng, P.; Pine, D.; Chmelka, B. F.; Whitesides, G. M.; Stucky, G. D., Hierarchically Ordered Oxides. *Science* **1998,** 282, (5397), 2244-2246.

13. Du, P.; Li, M.; Douki, K.; Li, X.; Garcia, C. B. W.; Jain, A.; Smilgies, D. M.; Fetters, L. J.; Gruner, S. M.; Wiesner, U.; Ober, C. K., Additive-Driven Phase-Selective Chemistry in Block Copolymer Thin Films: The Convergence of Top-Down and Bottom-Up Approaches. *Advanced Materials* **2004,** 16, (12), 953-957.

14. Auston, D. H.; Surko, C. M.; Venkatesan, T. N. C.; Slusher, R. E.; Golovchenko, J. A., Time-resolved reflectivity of ion-implanted silicon during laser annealing. *Applied Physics Letters* **1978,** 33, (5), 437-440.

15. Okabe, A.; Boots, B.; Sugihara, K.; Chiu, S. N., *Spatial Tessellations: Concepts and Applications of Voronoi Diagrams*. John Wiley & Sons: New York, 2000.

16. Segalman, R. A.; Hexemer, A.; Hayward, R. C.; Kramer, E. J., Ordering and Melting of Block Copolymer Spherical Domains in 2 and 3 Dimensions. *Macromolecules* **2003,** 36, (9), 3272-3288.

17. Jellison, G. E.; Lowndes, D. H.; Mashburn, D. N.; Wood, R. F., Time-resolved reflectivity measurements on silicon and germanium using a pulsed excimer KrF laser heating beam. *Physical Review B* **1986,** 34, (4), 2407.

18. Jellison, G. E.; Lowndes, D. H.; Sharp, J. W., Time-resolved optical studies of oxide-encapsulated silicon during pulsed laser melting *Journal of Materials Research* **1988,** 3, (3), 498-505.

19. Poate, J. M.; Mayer, J., *Laser Annealing of Semiconductors*. Academic Press: New York, 1982.

20. Thompson, M. O.; Galvin, G. J.; Mayer, J. W.; Peercy, P. S.; Poate, J. M.; Jacobson, D. C.; Cullis, A. G.; Chew, N. G., Melting Temperature and Explosive Crystallization of Amorphous Silicon during Pulsed Laser Irradiation. *Physical Review Letters* **1984,** 52, (26), 2360.

21. Li, J. G.; Hausner, H., Wetting and adhesion in liquid silicon/ceramic systems. *Materials Letters* **1992,** 14, (5-6), 329-332.

22. Hamley, I. W., *The physics of block copolymers*. Oxford University Press: New York, 1998.

23. Voyles, P. M.; Grazul, J. L.; Muller, D. A., Imaging individual atoms inside crystals with ADF-STEM. *Ultramicroscopy* **2003,** 96, 251-273.

CHAPTER 4

EPITAXIAL NiSi TABLE-LIKE FILMS ON SINGLE CRYSTAL SUBSTRATES BY LASER ANNEALING OF BLOCK COPOLYMER DERIVED POROUS THIN FILMS[3]

Abstract

Heteroepitaxy, the growth of a single orientation of a crystal over a crystalline substrate of other material, remains a challenge even for materials with a moderate lattice mismatch. Films develop misfit dislocations to accommodate the lattice mismatch resulting in large defect densities, and unstable film growth. Stable films might, however, be made if the epitaxial seeds were confined to small pores with the lattice allowed to relax as growth proceeds out of the pore, ultimately resulting in a defect-free crystalline film with a relaxed lattice at the surface. Here we demonstrate proof of this concept by growing nickel silicide heteroepitaxially on silicon substrates using a porous aluminosilicate template. These templates, with hexagonally arranged pores spaced 34.6 nm apart, were derived from block copolymer self assembly. Stoichiometric NiSi, UHV sputter deposited on the aluminoslicate templates, was laser annealed at fluences between 300 mJ/cm^2 and 700 mJ/cm^2. The resulting NiSi table-like films were near single crystal with 2 orthorhombic epitaxial orientations of grains on Si, rotated 90° in-plane from each other.

[3] Hitesh Arora, Sarmita Majumdar, Jerome Hyun, David Muller, Karen Kavanagh, Ulrich Wiesner, Michael Thompson. *To be submitted*

Introduction

Silicon remains to be the material of choice for semiconductor based devices, however, in order to overcome its limitations, other materials need to be grown on Si. Heteroepitaxy, growth of oriented crystal of material on other crystalline material, enables this by having an intimate contact between 2 different materials with some crystal planes pointing in a common direction. Heteroepitaxial films on Si typically have defects due to lattice mismatch and/or thermal mismatch. Only a certain amount of strain can be accommodated by any material without generating defects or dislocations. This thickness, known as Matthews-Blakeslee critical thickness limit, is typically several nanometers above which the strain in the films is relieved through defects or dislocations. It is, however, possible to eliminate dislocations by limiting the extent of epitaxy as shown for nanowires[1, 2] and by growth inside the pores[3]. The strain relaxation in this case occurs through lattice dilation over a few nanometers from the surface.

Metal contacts on silicon are useful for interconnects and contact pads. The low resistivity NiSi phase is currently of great interest for contacts in semiconductor devices due to its low temperature processing, low resistivity and low consumption of Si[4, 5]. The Ni-Si binary phase diagram is complex and has a variety of phases forming at different temperatures (Fig. 4.1). Six of these phases (Ni_3Si, $Ni_{31}Si_{12}$ or Ni_5Si_2, Ni_2Si, NiSi and $NiSi_2$) are known to be stable at room temperature with Ni_2Si, NiSi, $NiSi_2$ commonly observed in thin film reactions[6]. This increases the complexity of phase formation and its possible dependence on processing parameters and substrate variations such as dopant concentration, cleaning conditions. Typically, silicides are prepared through rapid thermal annealing (RTA) of thin films of Ni deposited on clean Si substrates. Thermal annealing causes a reaction between Ni and Si generating a complex phase sequence of nickel silicide formation[7, 8]. The NiSi phase is not in

equilibrium with Si and, at higher temperatures, it coverts into $NiSi_2$ [9]. Thinner NiSi films also tend to degrade at high temperatures through grain boundary grooving and agglomeration[10-12]. It is for these reasons that the processing conditions for the films needs to be carefully controlled. In a recent publication, morphological stability was achieved through alloying of the deposited Ni film with 40% Si resulting in large grain sizes[13].

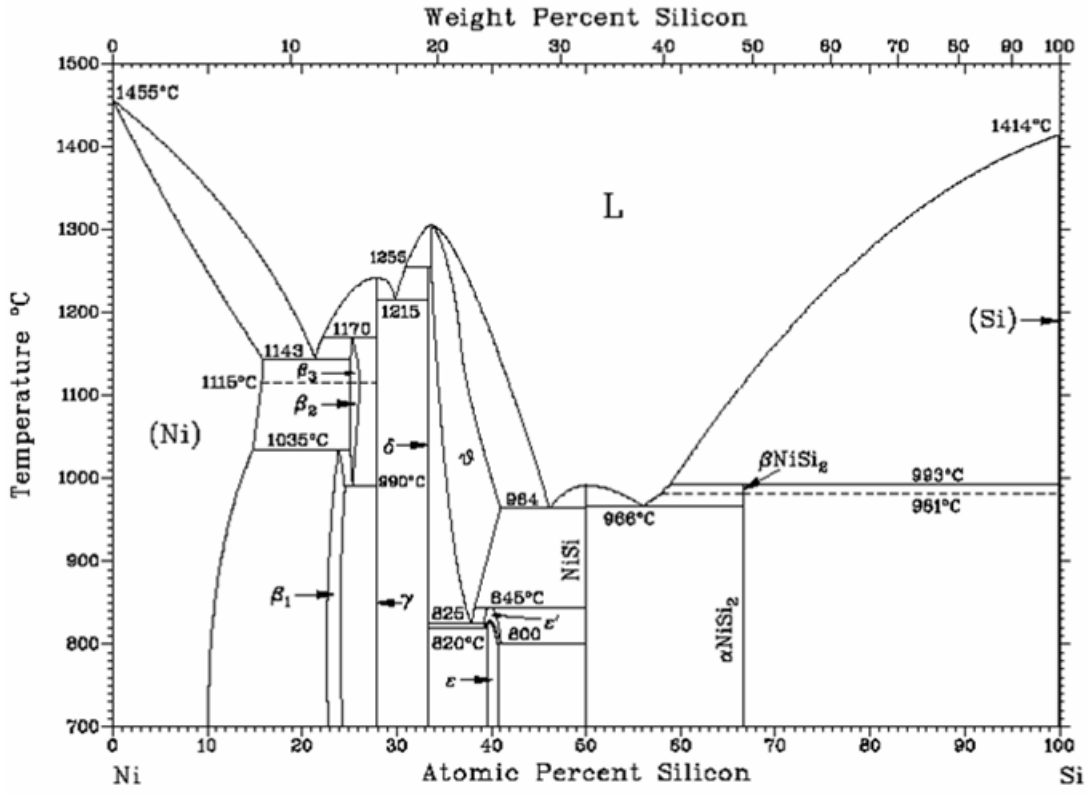

Figure 4.1: Binary phase diagram of Ni-Si.

Here, we demonstrate growth of a stable NiSi film within the pores and over a block copolymer derived porous template, resulting in a crystalline NiSi table-like film. Stoichiometric NiSi was UHV sputter deposited on Si substrates with block copolymer derived porous aluminosilicate templates. NiSi, melting temperature at

992 °C, was annealed in the liquid phase using an excimer pulsed laser to crystallize the amorphous as-deposited film remaining below the melt threshold of Si (1400 °C). This minimizes Ni diffusion into the substrate and prevents the consumption of Si to form Si rich phases. Upon laser annealing, epitaxy initiates from the pore with a strained lattice to match the Si lattice. With the absence of any lateral constraints, the film relaxes until reaching its equilibrium lattice structure. As the epitaxy grows out of the pore and over the template, crystals growing out of individual pores merge in collision boundaries. The growing grains are relaxed and the collision boundaries are not expected to be grain boundaries as long as the initial epitaxial alignment is the same and growth distances are small. In the case of orthorhombic NiSi on cubic Si, two equivalent epitaxial orientations exist and some of the collision boundaries will become grain boundaries between these orientations.

Crystal structure and orientation on Si(100) substrates

NiSi has an orthorhombic crystal structure (Fig. 4.2) with lattice constants: a = 5.233 Å, b = 3.258 Å, c= 5.659 Å[14]. These lattice constant values are for films made using deposited Ni on Si and are not equilibrium values[15]. The equilibrium values of lattice constant reported are: a = 5.1752 Å, b = 3.321 Å, c = 5.6094 Å[16] and are more relevant to our case. The melting point for NiSi is 992°C and, typically via solid state reactions forms around 350-400°C for deposited thin Ni films on Si. The NiSi films on Si have been found to have a unique off-normal fiber-like texture called as axiotaxy (an intermediate between heteroepitaxy and a random growth) resulting in a one-dimensional periodic interface with the NiSi(202), (211), (103), (112) planes aligned at a tilt to Si(220) planes since the projected spacing between these planes is almost identical to projected Si(220) spacing [17-19]. The net lattice mismatch with above orientations is 0.5-0.6 %.

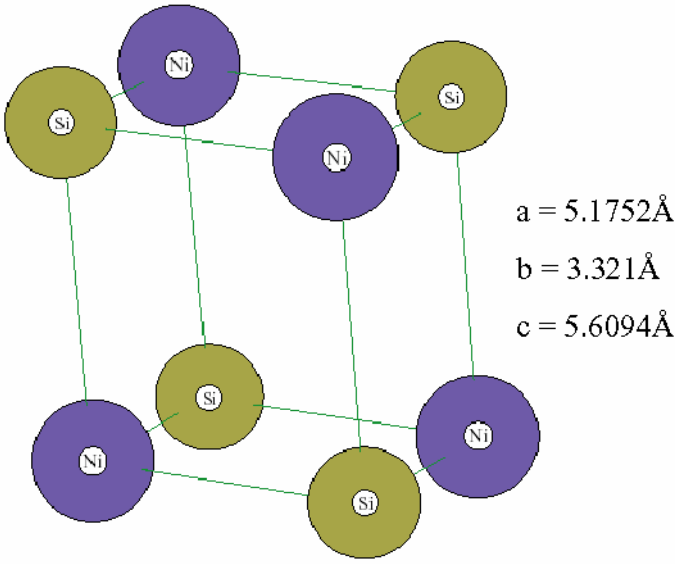

Figure 4.2: Crystal structure of NiSi with lattice parameters.

Experimental section

Materials and processing

Block copolymer derived porous aluminosilicate thin films were generated as described elsewhere[20]. The films were typically 15 nm thick with a pore spacing of 34.6 nm. 17 nm of 1:1 atomic ratio of Ni and Si was sputter deposited in a UHV chamber after a short *in-situ* ion etch to remove any native oxide at the bottom of the pore. The rate of deposition was calibrated using a crystal monitor. The samples were then laser annealed using a homogenized 30 ns XeCl excimer pulse laser at fluence between 300-700 mJ/cm^2. The excimer fluences were calibrated using surface reflectance of a bulk Si melt threshold at 600 mJ/cm^2.

Characterization

2-point resistance measurements were performed on samples using IV probe station with tungsten probes spaced 1 mm apart. A Keck Field Emission SEM was

used with an in-lens detector at 5 KeV for imaging the as-deposited and annealed samples.

Sample for plan-view TEM were prepared using wedge polishing at 3° angle and a dual beam FEI Focused Ion Beam was used for preparing cross-section TEM samples. A protective carbon and platinum layer was deposited on the sample to prevent damage to the NiSi film from the FIB. A Tecnai F-20 STEM, operated at 200 KeV, was used to image cross-section samples while a Hitachi TEM at 100 keV was used for plan-view imaging and electron diffraction.

X-ray diffraction was collected using a rotating substrate with a constant incidence angle, see supporting information.

Results and Discussion

As deposited, sputtered NiSi (1:1) films were conformal to the porous structure of the underlying template, with SEM images showing weak contrast from the underlying template. After pulse laser induced metling, films remain similarly smooth with no signs of agglomeration when observed under SEM, see Fig. 4.3a.

Resistance measurements were performed across samples as a function of the laser fluence. The 2-point resistance (Fig. 4.3b) exhibited a dramatic drop for fluence above 400 mJ/cm^2, indicating the formation of low resistivity crystalline NiSi. At higher fluences the resistance remains unchanged suggesting a stable film formation. The absolute value of the NiSi film resistivity could not be determined due to the complicated table-like film (an oxide template between NiSi and Si) geometry and expected film thinning on top of the porous template. Nevertheless, qualitative trend of resistance variation with fluence is expected to be similar and the 2x drop in resistance with increasing fluence is consistent with that observed by others in the low temperature processing range[13].

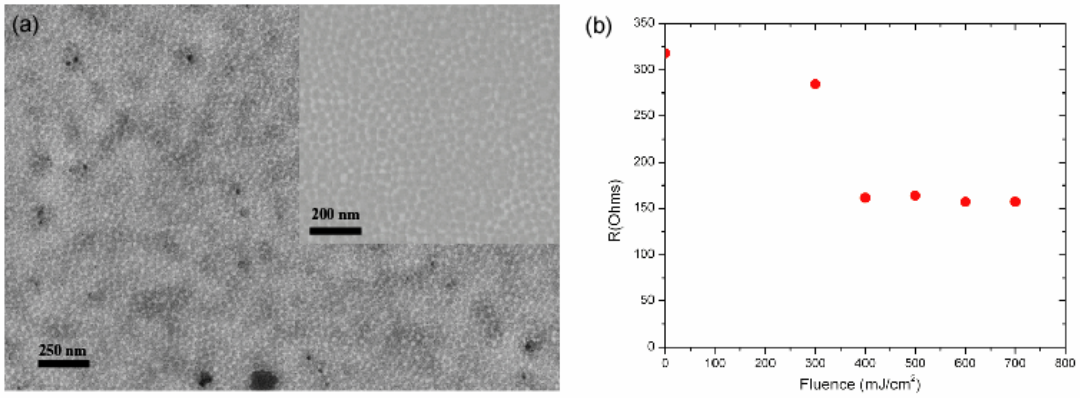

Figure 4.3: (a) SEM image of 17 nm NiSi thin film after laser annealing at 550 mJ/cm^2. Inset shows SEM image of the as-deposited film. (b) Resistance of films annealed at fluence between 300-700 mJ/cm^2.

Selected area electron diffraction and plan-view TEM, along Si(220) and Si($\underline{2}$20) direction, on a wedge polished sample are shown in Fig. 4.4. Electron diffraction confirmed near single crystal orientation with no evidence of polycrystalline rings (Fig. 4.4d). Indexing of reflections from the NiSi film indicate an epitaxial orientation of the NiSi b-axis parallel to Si[110] and NiSi[101] parallel to Si[1$\underline{1}$0]. Because of the orthorhombic crystal geometry, there are 2 equivalent relaxed orientations of the pseudo-cubic NiSi that grows from the Si. The two orientations, shown in Fig. 4.4c, are just rotated 90° from each other about the surface normal. Calculated diffraction pattern from these orientations match experimentally observed reflections (Fig. 4.4e). This orientation was also confirmed through X-ray diffraction on a large area of the sample, with diffraction observed from NiSi(211), NiSi(020), Si(311) planes and an overlap of reflections from the NiSi(202) and Si(220) planes (see supporting information Fig. 4.S2). Due to the limited resolution of the detector (~0.1Å), the reflections from the planes of two different orientations could not be resolved. Therefore, the diffraction spot pattern only indicates presence of near-single crystal and absence of polycrystalline orientations in the NiSi film.

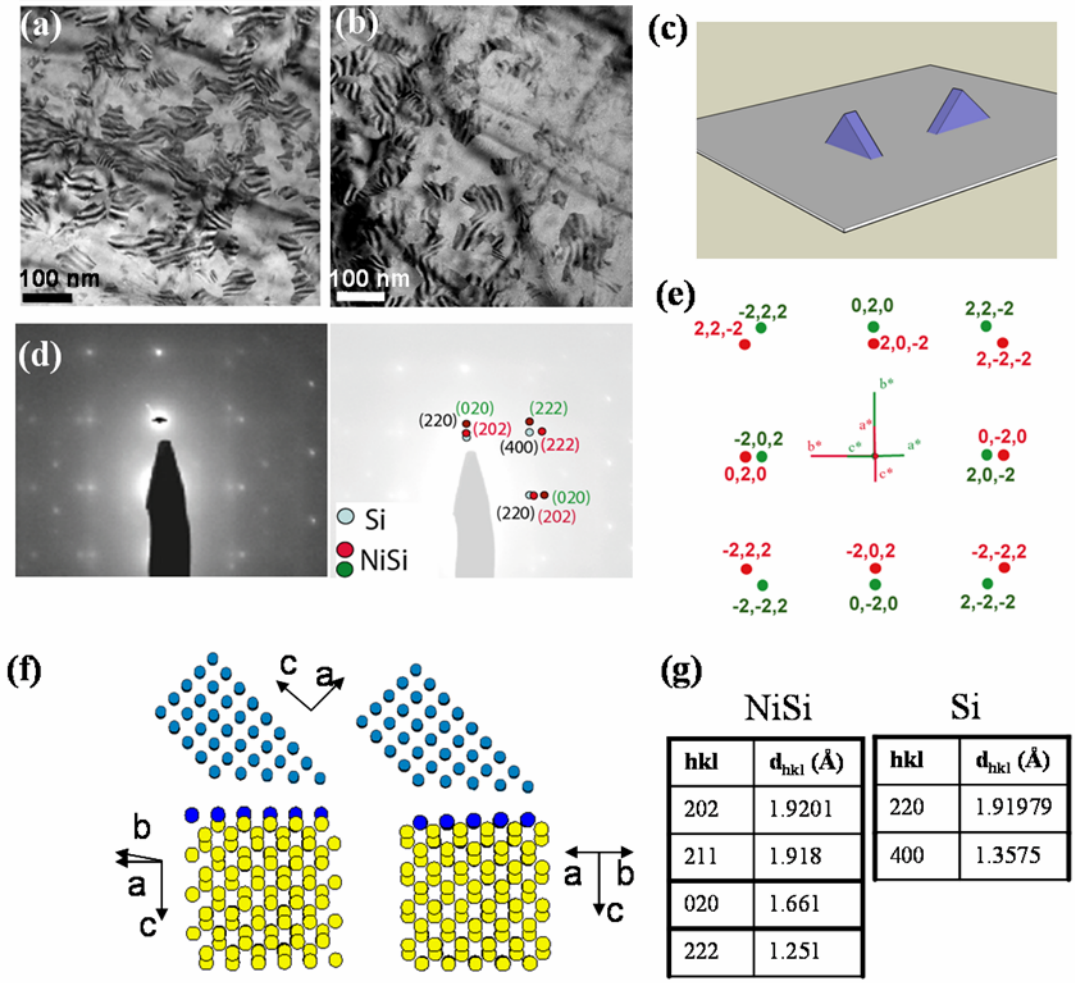

hkl	d_{hkl} (Å)
202	1.9201
211	1.918
020	1.661
222	1.251

hkl	d_{hkl} (Å)
220	1.91979
400	1.3575

Figure 4.4: (a)-(b) Plan-view TEM images of a film annealed at 550mJ/cm^2 taken along Si(220) and Si(2̲20) zone axis. (c) Schematic showing NiSi orientations on Si substrate (cuboid on cube geometry). (d) Selected area electron diffraction pattern corresponding to TEM image in (a), with reflections from two orientations indexed. (e) Calculated electron diffraction from two orientations of NiSi film on Si. (f) Two NiSi lattice orientations on Si(1̲10) and Si(110) projection. (g) d-spacing for relevant NiSi and Si planes.

The plan-view TEM along the Si(220) and Si(2̲20) zone axis also indicates 2 orientations of NiSi grains with 2 sets of Moiré fringes oriented 90° in plane, with a spacing of ~ 20 nm, see Fig. 4.4a-c. These translational Moiré fringes are due to interference from NiSi(202) plane overlaying Si(220) planes, calculated using the relation between plane spacing and fringe spacing:

$$d_m = \frac{d_1 d_2}{(d_1 - d_2)} \sim 20nm$$

where d_1 and d_2 are the plane spacing of the Si(220) and NiSi(202). These two orientations with 90° rotations are explained by the 2 possible orientations of the relaxed NiSi lattice. The symmetry of an orthorhombic crystal (cuboid geometry) allows the strained cubic lattice to relax into 2 orientations, 90° apart, with a-axis (and c- axis) of 2 orientations in perpendicular direction (Fig. 4.4f).

Cross-section STEM of the NiSi-Si interface also confirms epitaxial alignment within the pores of the template (Fig. 4.5). The lattice over the top of the template (overgrowth) showed fringes in the vertical direction only, likely due to sample curling about a horizontal axis. Presence of Ni in the pillar and overgrowth was confirmed by EELS with the spectra on the pillar and overgrowth showing a clear evidence of the Ni L-edge at 860 eV.

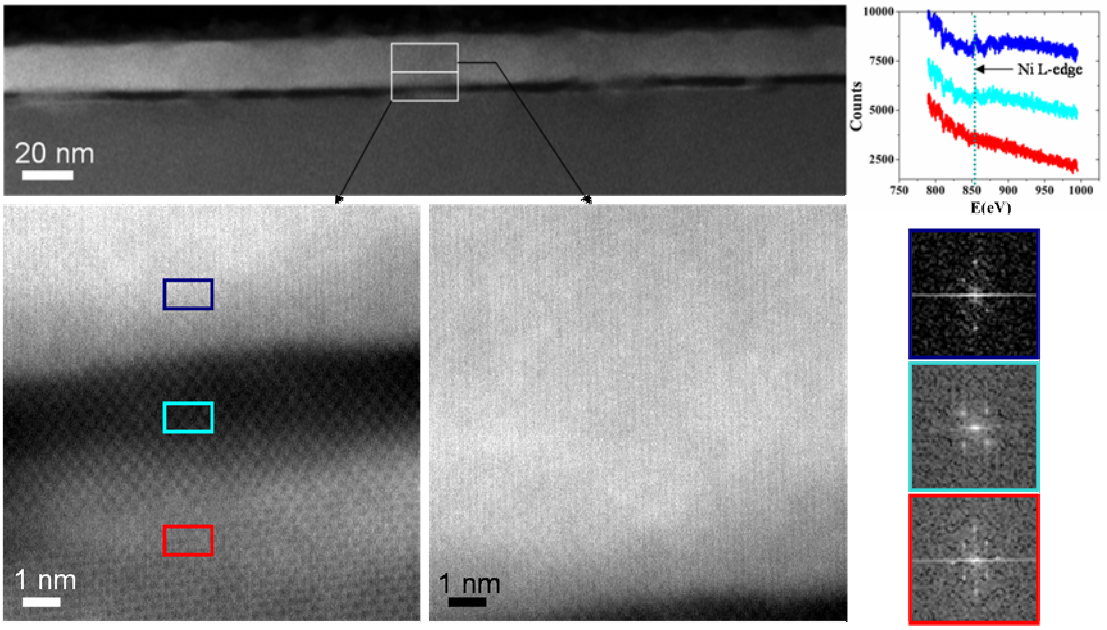

Figure 4.5: STEM images of the cross-section of the sample annealed at 550 mJ/cm^2, with FFT and EELS data on the substrate, pillar, and overgrowth.

At higher fluences, above 650 mJ/cm^2, the underlying Si can be incorporated into the liquid and significant silicide was observed under the template, suggesting that a significant amount of molten silicide flows under the template when annealed at higher temperatures, see Fig. 4.S3. We believe this is due to surface force driven flow of molten silicide on the oxide template, driving the template towards the surface. Twinning defects were observed at the NiSi-Si interface in this case likely arising from NiSi crystallization over large areas without the confinement of the pores.

In summary, block copolymer derived porous aluminosilicate templates were used to generate crystalline NiSi tables on single crystal Si substrates. Upon laser annealing, crystal growth proceeded epitaxially from the bottom of the pore, with NiSi crystals grown pseudomorphically. As the strain is relieved during growth through the pores, the NiSi crystal relaxed into 2 orientations with NiSi[101] parallel to the Si[1$\underline{1}$0] and NiSi[010] parallel to Si[110]. The NiSi films obtained showed good morphological stability. Such crystalline table-like structures on single crystal structures may provide excellent platforms for generating large scaled areas of single or near-single crystal epitaxial nanostructured surfaces. Removal of aluminisilicate template would also yield galleries of crystalline NiSi and may open opportunities for fundamental studies in nanofluidics.

Acknowledgements

The authors acknowledge financial support of this research by NSF (DMR-0404195) through the NIRT program. The research made use of facilities of Cornell Center for Materials Research (CCMR) with funding from the Materials Research Science and Engineering Center program of NSF (cooperative agreement DMR-0520404), Cornell Nanobiotechnology Center (NBTC) supported in part by the STC

Program of the National Science Foundation under Agreement No. ECS-9876771 and Cornell Nanoscale Facility (CNF) supported by the National Science Foundation under Grant No. ECS-0335765.

APPENDIX C

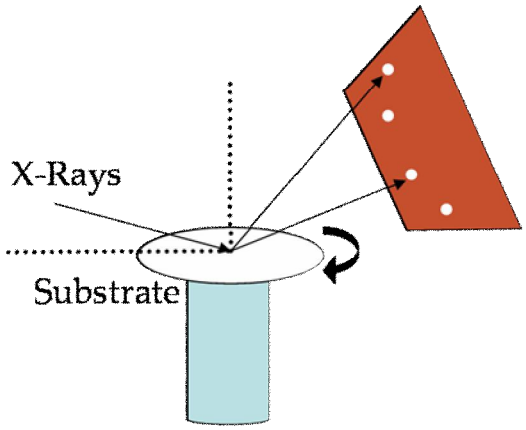

Figure 4.S1: Illustration to show sample geometry for X-ray diffraction in the GADDS system.

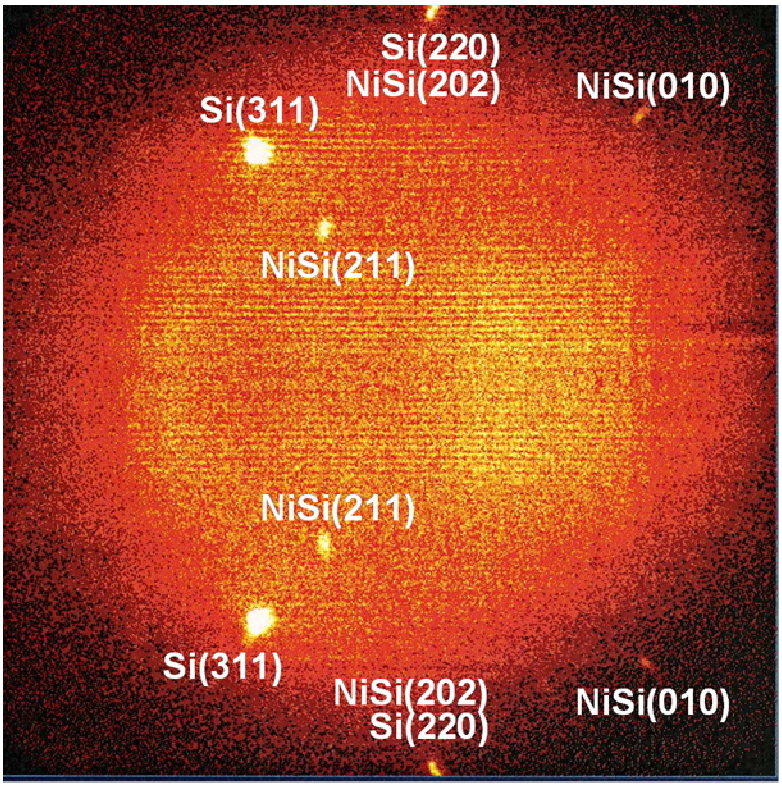

Figure 4.S2: 2-D X-ray Diffraction pattern of a sample annealed at 550 mJ/cm^2 using the GADDS system.

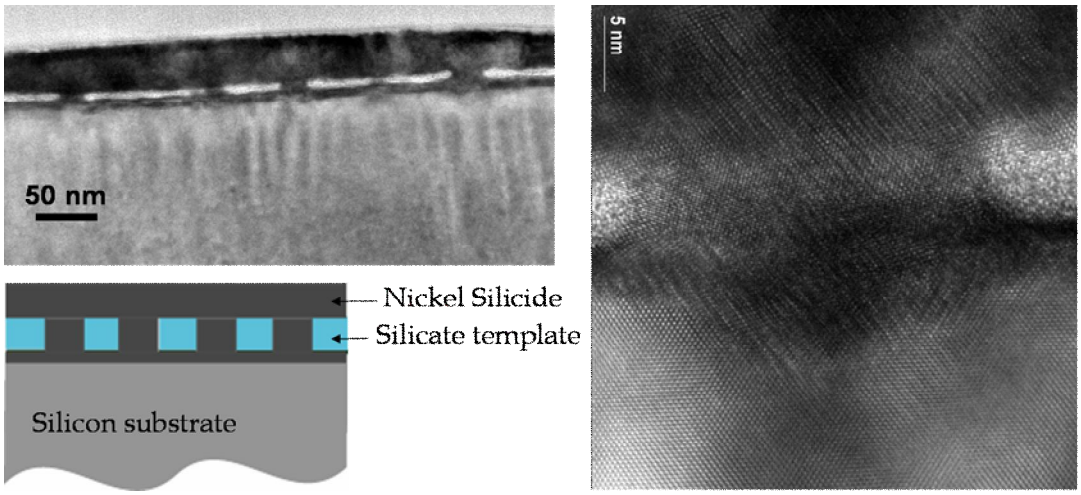

Figure 4.S3: HRTEM of a sample annealed at 650 mJ/cm^2. Schematic showing position of different materials observed in the TEM of the sample.

REFERENCES

1. Kamins, T. I.; Li, X.; Williams, R. S.; Liu, X., Growth and Structure of Chemically Vapor Deposited Ge Nanowires on Si Substrates. *Nano Letters* **2004,** 4, (3), 503-506.

2. Wu, Y.; Xiang, J.; Yang, C.; Lu, W.; Lieber, C. M., Single-crystal metallic nanowires and metal/semiconductor nanowire heterostructures. *Nature* **2004,** 430, (6995), 61-65.

3. Park, J. S.; Bai, J.; Curtin, M.; Adekore, B.; Carroll, M.; Lochtefeld, A., Defect reduction of selective Ge epitaxy in trenches on Si(001) substrates using aspect ratio trapping. *Applied Physics Letters* **2007,** 90, (5), 052113-3.

4. Chen, L. J., *Silicide Technology for Integrated Circuits*. The Institution of Electrical Engineers: London, UK, 2004; p 95-151.

5. Murarka, S. P., *Silicides for VLSI applications*. Academic Press: New York, NY, 1983.

6. Moffatt, W. G., *The handbook of binary phase diagrams* Genium Pub. Corp. : Schenectady, N.Y. , 1976

7. Tinani, M.; Mueller, A.; Gao, Y.; Irene, E. A.; Hu, Y. Z.; Tay, S. P., In situ real-time studies of nickel silicide phase formation. *Journal of Vacuum Science & Technology B: Microelectronics and Nanometer Structures* **2001,** 19, (2), 376-383.

8. Lavoie, C.; Purtell, R.; Coia, C.; Detavernier, C.; Desjardins, P.; Jordan-Sweet, J.; Cabral, C., Jr. ; d'Heurle, F. M.; Harper, J. M. E., In situ monitoring of thin film reactions during rapid thermal annealing: Nickel silicide formation. *Proceedings - Electrochemical Society* **2002,** 2002-11, 455-467.

9. Detavernier, C.; Ozcan, A.; Lavoie, C.; Sweet, J.-J.; Harper, J. M. E., Kinetics of agglomeration of NiSi and NiSi2 phase formation. *Materials Research Society Symposium Proceedings* **2003,** 745, 135-140.

10. Chamirian, O.; Kittl, J. A.; Lauwers, A.; Richard, O.; van Dal, M.; Maex, K., Thickness scaling issues of Ni silicide. *Microelectronic Engineering* **2003,** 70, (2-4), 201-208.

11. Lauwers, A.; Steegen, A.; de Potter, M.; Lindsay, R.; Satta, A.; Bender, H.; Maex, K., Materials aspects, electrical performance, and scalability of Ni silicide towards sub-0.13 mu m technologies. *Journal of Vacuum Science & Technology B: Microelectronics and Nanometer Structures* **2001,** 19, (6), 2026-2037.

12. Mukai, R.; Ozawa, S.; Yagi, H., Compatibility of NiSi in the self-aligned suicide process for deep submicrometer devices. *Thin Solid Films* **1995,** 270, (1-2), 567-572.

13. Van Bockstael, C.; De Keyser, K.; Van Meirhaeghe, R. L.; Detavernier, C.; Jordan-Sweet, J. L.; Lavoie, C., Influence of a transient hexagonal phase on the microstructure and morphological stability of NiSi films. *Applied Physics Letters* **2009,** 94, (3), 033504-3.

14. JCPDS. No. 38-0844.

15. Detavernier, C.; Lavoie, C.; d'Heurle, F. M., Thermal expansion of the isostructural PtSi and NiSi: Negative expansion coefficient in NiSi and stress effects in thin films. *Journal of Applied Physics* **2003,** 93, (5), 2510-2515.

16. Rabadanov, M. K.; Ataev, M. B., Refinement of the Structure of Nickel Monosilicide Crystals. *Inorganic Materials* **2002,** 38, (2), 120-123.

17. Detavernier, C.; Ozcan, A. S.; Jordan-Sweet, J.; Stach, E. A.; Tersoff, J.; Ross, F. M.; Lavoie, C., An off-normal fibre-like texture in thin films on single-crystal substrates. *Nature* **2003,** 426, (6967), 641-645.

18. Detavernier, C.; Jordan-Sweet, J.; Lavoie, C., Texture of NiSi films on Si(001), (111), and (110) substrates. *Journal of Applied Physics* **2008,** 103, (11), 113526-9.

19. Alberti, A.; Bongiorno, C.; Cafra, B.; Mannino, G.; Rimini, E.; Metzger, T.; Mocuta, C.; Kammler, T.; Feudel, T., Pseudoepitaxial transrotational structures in 14 nm-thick NiSi layers on [001] silicon. *Acta Crystallographica Section B* **2005,** 61, (5), 486-491.

20. P. Du; M. Li; K. Douki; X. Li; C. B W Garcia; A. Jain; D. M. Smilgies; L. J Fetters; S. M Gruner; U. Wiesner; Ober, C. K., Additive-Driven Phase-Selective Chemistry in Block Copolymer Thin Films: The Convergence of Top-Down and Bottom-Up Approaches. *Advanced Materials* **2004,** 16, (12), 953-957.

CHAPTER 5

EARTHWORM INSPIRED LOCOMOTIVE MOTION FROM FAST SWELLING HYBRID HYDROGELS[4]

Abstract

Diverse motion mechanisms encountered in nature serve successfully as a guide for engineering efficient mobile devices used in cargo transport and force generation. We have previously demonstrated earthworm locomotion inspired directed motion and cargo transport using a pNIPA hydrogel based device. The motility mechanism involved sequential shrinking and swelling of segments of a long gel in a glass capillary, induced by volume phase transitions, through a simple temperature stimulus using peltier elements. The same effect is generated in the earthworm by flexing and stretching muscles along the body as it moves in its underground burrow. The shrinking segments move the body forward while the swollen segments anchor against the walls to prevent slippage. Here we show an improved device, using the same working principle, made of super-porous, mechanically robust organic-inorganic hybrid hydrogels (also known as nanocomposite hydrogels) which show large volume phase transitions above 32°C without requiring lengthy hydrolysis times. The gels demonstrate fast swelling kinetics with complete restoration of their initial size in short times, making the gels reusable for multiple cycles. This improved device, with its reusability, fast swelling kinetics and efficient slip-free motion, opens a variety of possibilities for applications in microfluidics, nanobiotechnology, small scale robotics and MEMS.

[4] Reproduced with permission from: Hitesh Arora, Rahul Malik, Lilit Yeghiazarian, Claude Cohen, Ulrich Wiesner. *Journal of Polymer Science, Part A: Polymer Chemistry*, (2009), 47 (19), 5027-33.

Introduction

Transformation of energy into directed motion requires different forms of complexity at different length scales. Nature demonstrates several mechanisms for inducing motion, at different length scales, in various organisms. Incorporating these mechanisms into microfluidics, micro electro mechanical systems (MEMS) and drug delivery systems for efficient directional motion and transport may fulfill the needs of these ever advancing fields. Although devices based on biological systems have demonstrated that directed motion can be induced using e.g. adenosine triphosphate (ATP) powered biomolecules such as motor proteins, the stringent physiological conditions required limit the applicability of such systems. The most promising biological approach is an inverted motility assay where the substrates are coated with Kinesin motor proteins. Directed motion of the microtubules was generated when Kinesin molecules, powered through hydrolysis of ATP molecules, "walk" on the microtubules with discrete 8-nm steps[1, 2]. Their charged ends have also been used to change the direction of motion upon applying external electric fields, a feature that has shown potential for molecular sorting[3]. Similar feat has been achieved by functionalizing microtubule segments with magnetic nanoparticles and applying external magnetic fields to steer the transport direction[4]. While these are fascinating approaches for inducing motion and cargo transport in a device using biomolecules, the stringent environmental conditions required and complexity involved in integration with the synthetic components of the device often limits their usability. In contrast, a responsive synthetic material, that can endure more severe conditions, may provide the necessary robustness and more freedom to tune parameters as per the requirement. Synthetic materials such as hydrogels that respond to changes in the environment such as pH[5, 6], temperature[7, 8], electric field[9] and light[10] are ideal for such devices. The

responsive nature of these hydrogels has been exploited to make devices useful for applications ranging from biotechnology[11, 12] to microfluidics[13, 14].

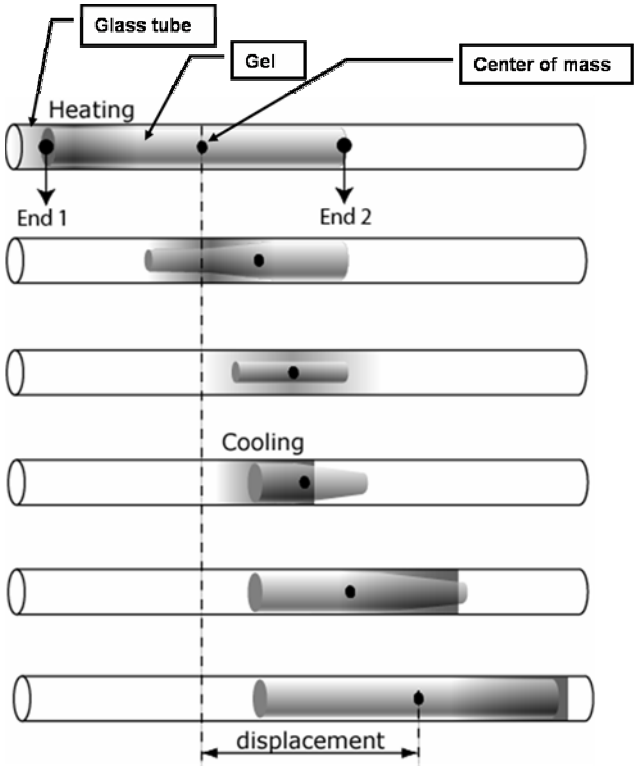

Figure 5.1: Schematic showing the mechanism of motion of cylindrical gels inside a capillary tube.

Previously, we developed a prototype device based on thermoresponsive N-isopropylacrylamide (NIPA) hydrogels (lower critical solution temperature (LCST) ~ 32°C) that mimicked the earthworm locomotion[15]. The motility mechanism of our gel based device involved sequentially shrinking and swelling the segments of a cylindrical gel in a glass capillary, induced by volume phase transitions through simple temperature stimuli applied along the gel using peltier elements, see Fig. 5.1. The symmetry is broken by moving the locally induced phase transition from one end of the gel (end 1) to the other end (end 2) rather than applying it over the entire gel, thus generating forward motion of end 1 (shrinking cycle). Subsequent sequential

swelling of the segments, by reversing the stimulus, from the same end brings the gel to the original size and generates motion of the end 2, in the same direction (swelling cycle). A similar mechanism of locomotion is shown by an earthworm flexing and stretching muscles along its body to generate the same effect as shrinking and swelling in our case. The shrinking segments move the body forward while the swollen segments hold the surface to prevent the moving body from slipping. The initial device, capable of generating directed motion at velocities of the order μm/sec and cargo carrying capability, had limitations, however, pertaining to long hydrolysis times to induce large volume changes, low mechanical robustness of the moving parts, slow swelling kinetics and slippage at the walls leading to imperfect motion. Here we show a new device, based on the same working principle, which overcomes these challenges. The device is made of super-porous, organic-inorganic hybrid hydrogels that show large volume phase transitions above 32°C without requiring additional hydrolysis and show fast swelling kinetics that allow the gels to regain their initial size in short times. Additionally, by roughening the capillary walls through acid treatment and using smaller sized peltier elements, we were able to generate efficient slip-free motion, over multiple cycles and with velocities of order μm/sec. The mechanism shown here is different from other gel based devices where the motion is induced by using anisotropic substrates to break the symmetry[16-18]. In our case, symmetry breaking occurs through propagation of volume phase transitions over a long cylindrical gel, Fig. 5.1. We believe this significantly improved device, with efficient motion generation, will enable incorporation of this mechanism of motion into devices useful for various applications including sensors, pumps, cargo transport and cavity exploration[19].

Experimental Section

Hybrid gel synthesis

Hybrid NIPA gels were synthesized as described elsewhere[20]. Laponite XLG clay particles (30nm in diameter and 1 nm in thickness) were used as multifunctional physical crosslink points for the NIPA polymer chains grown through free radical polymerization. The clay (0.4 g) was first exfoliated by stirring in water (28.5 mL) for 30 min. after which the solution became clear. Then the NIPA monomer (3.5 g), purified by recrystallizing from hexane/toluene mixture, was dissolved. The initiation occurred at the face of clay particles as potassium persulphate (30 mg in 1.5 mL water) and *N*,*N*,*N*′,*N*′-tetramethylethylenediamine (24 μL) were added to the solution[20]. The radical polymerization then propagated to first form clay-brush particles which subsequently formed a network of NIPA chains crosslinked at the face of the clay particles[20]. Water was bubbled with N_2 for 3 hours prior to addition of all other chemicals and O_2 was prevented throughout the experiment.

Heat treatment for synthesizing "fast" hybrid gels

The capillaries, purchased from Chemglass with 1 mm in internal diameter, were injected with polymerizing solution and then kept in an oven at 50°C for 1 day. The gels were then washed with de-ionized water several times after which the capillaries were filled with water and sealed at the ends. The initial swollen gel length was typically between 2.5 to 4 cm.

Glass capillary treatment

The inside wall of the capillaries were roughened by immersing them in 48% hydrofluoric (HF) acid solution for 3 min. The capillaries were subsequently washed with water several times before injecting polymerizing solution in them.

SEM sample preparation and imaging

After synthesis the gels were taken out of the capillaries and washed several times with de-ionized water. The gels immersed in water and completely swollen in a glass vial were then cooled to liquid N_2 temperature and then dried under vacuum at -5°C for 2 days. The dried gels were sputter coated with a thin layer of Au-Pt. A Leica SEM was used at 5 KeV for imaging.

Peltier element (PE) devices for heating and cooling

Two separate prototype devices, with different sizes of peltier elements, were used for the experiments. The first had 9x9 mm^2 size peltier elements while the second had 4.2x4.2 mm^2 size elements. Each element was connected in a parallel circuit to the DC power supply through an ON-OFF-ON toggle switch so that the same peltier element surface could be used for heating and cooling by reversing the direction of the current[15]. A DC voltage of 1.5 V was applied across each PE and within 10-15 seconds the surface would heat up above the phase transition temperature of the gel.

Experimental setup and procedure

The setup included a series of peltier elements, over which the capillary with the gel rested. The size of the stimulated gel segment was typically ~ 1 mm larger than the size of the peltier element due to heat transfer in the longitudinal direction of the capillary and depended on the power supplied to the peltier elements. For standard gels, each segment was typically heated for 9 min. to ensure complete shrinking before heating the next segment. For their swelling cycles, the segments needed to be cooled for several hours before regaining their initial length. In the case of fast swelling gels, each gel segment was heated for 5 min. before heating the next segment. In their

swelling cycles, segments needed to be cooled for 9 min. before they regained their initial length.

Results and discussion

Robust Gel chemistry

Standard NIPA gels with organic crosslinker (referred to as "standard gels" from hereon) are limited in their use due to poor mechanical properties[21] and slow hydrolysis times[6], which are typically several days, to generate large discontinuous volume changes upon phase transitions. In our previous experiments, standard gels were limited in their reusability during several shrinking and swelling cycles. Often gels would not come back to their full initial length and would stall after one or two cycles. In contrast, NIPA-clay based gels (referred to as "hybrid gels" from hereon) were reusable and showed remarkable mechanical properties due to the presence of inorganic clay particles[20, 21], making them more suitable for applications involving cargo transport. Additionally, the hybrid gels were alleviated from the need of hydrolysis, showing large volume changes upon increasing the temperature above their lower critical solution temperature (LCST), without additional hydrolysis. This was extremely advantageous as unlike standard NIPA gels the gels could be used immediately after their synthesis.

The polymerizing solution for hybrid gels was injected into glass capillaries (diameter = 1 mm) with the final swollen gel length between 2.5-4.0 cm. After a few washing steps to remove unreacted monomer, the gels were placed over a series of 9x9 mm^2 PE devices, see the experimental section. The length of the gel was monitored as it underwent shrinking and swelling cycles. In contrast to standard gels, the hybrid gels derived from exfoliated clay nanoparticles and NIPA were taken through several

shrinking and swelling cycles with full length recovery at the end of all the cycles, as shown with three shrinking and swelling cycles in Fig. 5.2a.

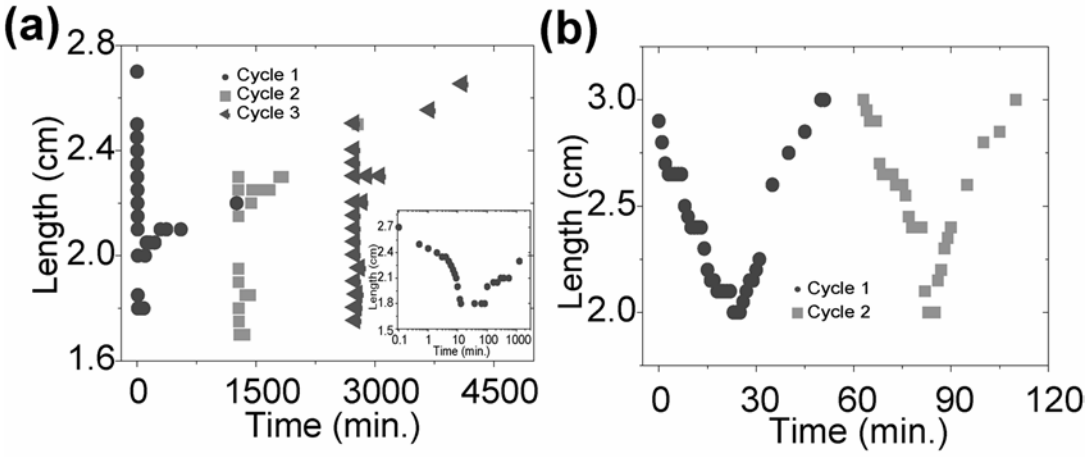

Figure 5.2: Variation of gel length with time during shrinking and swelling cycles for: (a) standard hybrid gels, prepared at room temperature (inset is the first shrinking and swelling cycle with time on a log scale); (b) fast hybrid gels, prepared above the LCST of the gel.

Fast swelling kinetics

The gels for which the results in Fig. 5.2b were produced were not only robust but also were synthesized under special conditions to show fast swelling kinetics (they are hence referred to as "fast hybrid gels" hereafter). For conventional hybrid gels, the gel length decreased reasonably fast during shrinking cycles but increased very slowly during the swelling cycles: The shrinking cycle took close to 10 min. before the gel attained its completely collapsed length (~ 1.8 cm). The swelling cycle, in contrast, took ~ 900 min. to recover 77% of the initial gel length, see inset in Fig. 5.2a. The slow swelling kinetics is typical for hydrogels [22]. In the present case, however, the swelling of segments may have been additionally slower due to (i) physical constraints imposed by adjacent segments and the glass walls, (ii) due to the slow collective diffusion rates of gel through water and, (iii) possibly due to the formation of a thin

skin layer preventing water from easily reaching the core of the gel[23, 24]. There are several physical and chemical methods to improve gel swelling kinetics by introducing inhomogeneities, which form interconnected pores, or macro-porosity into the gel network[25]. In our system, for experimental simplicity, we introduced heterogeneities by synthesizing the "fast hybrid gels" above their LCST, see the experimental section. Above the LCST, the chains become insoluble in water and phase separate to form domains rich in water surrounded with pNIPA chains[26, 27]. This indeed led to fast swelling kinetics of the gels as shown in Fig. 5.2b. The variation of gel length with time upon two shrinking and swelling cycles clearly shows faster swelling kinetics with 100 % gel length recovery in close to 30 min. as compared to conventional hybrid gels (prepared at room temperature) with similar initial length and very similar crosslink density (L/l_o = 1.5 and 1.45 for standard and super-porous gel, respectively; where L is the initial length of the swollen gel and l_0 is the length of the shrunken gel) while retaining good reusability, compare inset in Fig. 5.2a and Fig. 5.2b.

SEM on freeze dried gel samples revealed that the pore structure is better defined and has higher pore density in fast hybrid gels as compared to the conventional hybrid gels prepared at room temperature, Figs. 5.3a-b. Although the SEM images suggest smaller pores in the gels synthesized above the LCST as compared to gels prepared at room temperature, the faster swelling kinetics can be explained if the synthesis at higher temperature leads to a higher number of interconnected pores forming channels that provide shorter routes for water entering the network, thus facilitating the gel swelling kinetics. Additionally, since both the conventional and fast hybrid gels have the same composition, it is likely that the latter have thinner walls which may also ease the penetration of water into the gel. It should be noted that the freeze-drying process can, in principle, lead to changes in pore structure and size from the original sample. These SEM images should thus only be used as a qualitative representation of

the pore structure on the surface of the gel that will allow water to penetrate into the gel. Pore sizes observed in these gels are consistent, however, with what was observed by others for fast swelling gels[25].

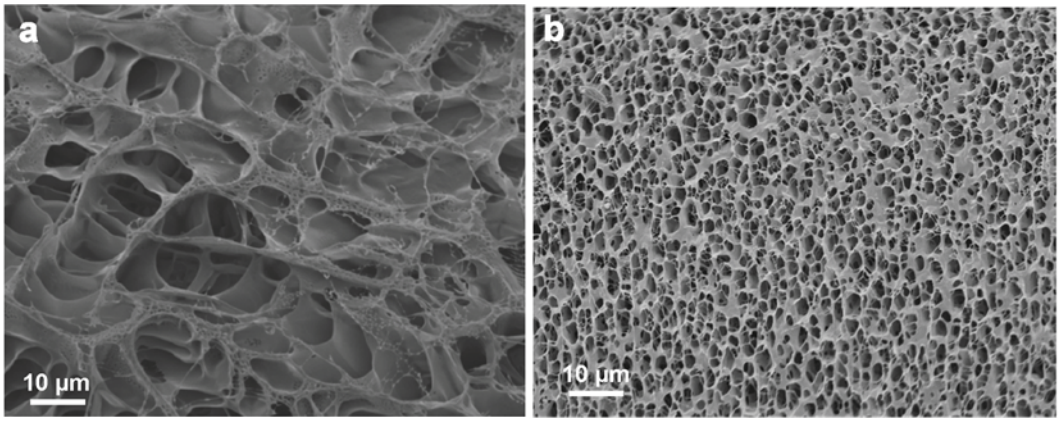

Figure 5.3: SEM images of freeze-dried samples of: (a) a standard hybrid gel, prepared at room temperature; (b) a fast hybrid gel, prepared above the LCST.

Reducing slippage at the capillary walls

In an earthworm, forward motion is generated by expansion of some segments while other segments hold on to the walls of the burrow. In our case, by following the ends of the fast hybrid gels with time during the shrinking and swelling cycles, we observed extensive slippage at the capillary walls, Fig. 5.4a-d. We categorize this slippage into 2 parts: (1) *slip1*: this slippage occurred at end 2 (right side of the gel in Fig. 5.4a-d) during shrinking cycles, Figs. 5.4a-b; and (2) *slip2*: this slippage occurred during swelling cycles where instead of only the second end, both ends moved towards the free surfaces, resulting in some degree of swelling in both directions, Figs. 5.4b-c. *Slip1*, where the end 2 moved backwards during last stages of the shrinking cycle, was due to weak adherence of the swollen gel to the capillary wall. As the last few segments of the gel shrink, the swollen segments of the gel slipped on the walls and were pulled backwards towards the already shrunken segments. *Slip2*, where the

gel swells in both directions, initiated with the swelling of the first segment backwards towards the free surface (end 1) and upon swelling of subsequent segments resulting in the gel being pushed equally in both directions. This was the result of the lack of friction between the swollen gel and the capillary wall.

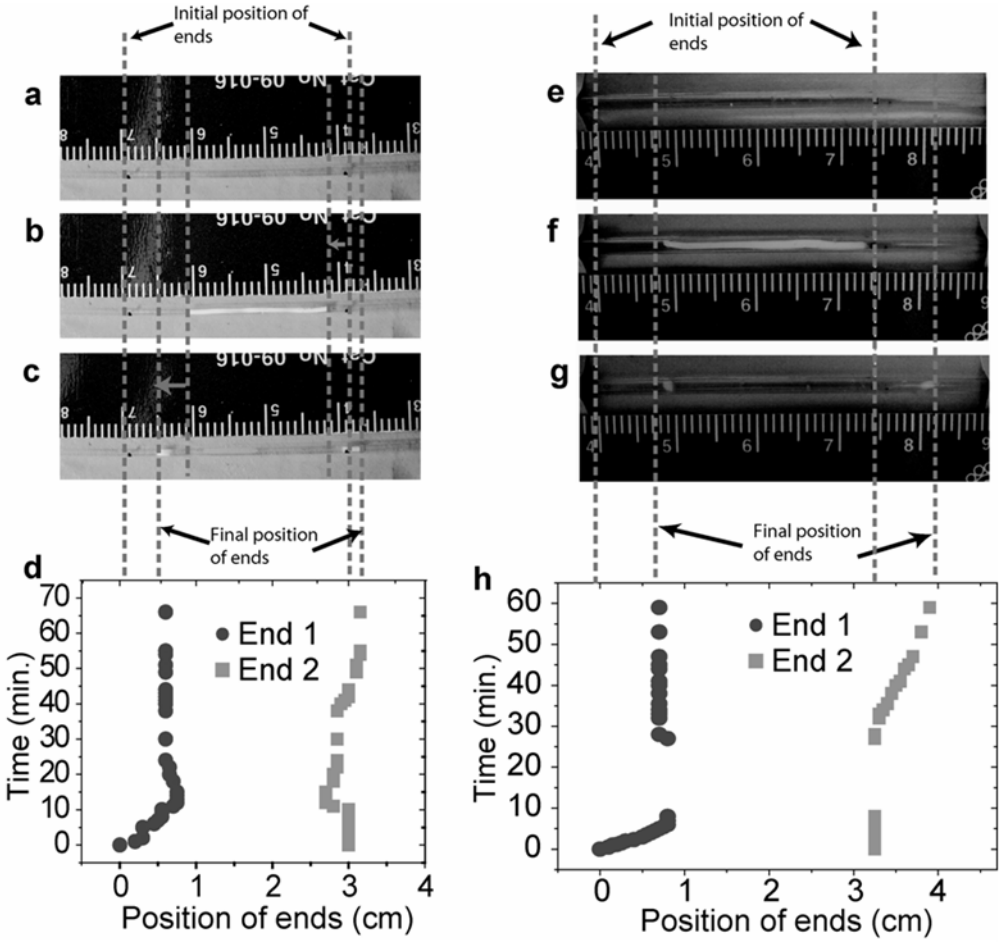

Figure 5.4: Snapshots of gel motion during shrinking and swelling cycles to show the slippage at the capillary walls with: (a-c) a fast hybrid gel inside untreated capillary; (e-g) a fast hybrid gel inside capillary with rough walls. Movement of ends of the gel with time during a shrinking and swelling cycle for a fast swelling hybrid gel inside; (d) an untreated capillary; (h) inside a capillary with rough walls. Grey arrows between vertical lines in snapshots indicate direction and magnitude of motion during slippage.

The overall slippage could be quantified by comparing forward motion of the center of the gel to the expected motion if there was no slippage (referred to as the

"ideal motion"). The forward motion with no slippage will result in gel center motion by $L-l_0$ after one shrinking and swelling cycle. The deviation from the ideal forward motion could be quantified as the fraction of distance traveled by the center of the gel in the forward direction over that in the ideal motion.

$$Slippage\ \ factor = 1 - \frac{\text{distance traveled by center of the gel in real motion}}{\text{distance traveled by center of the gel in ideal motion}}$$

A slippage factor of 0 would imply ideal forward motion and a factor of 1 would imply isotropic shrinkage and swelling resulting in no forward motion.

With the fast hybrid gels the slippage factor was determined to be ~ 0.7 when using capillaries as received, without any surface treatment, Fig. 5.4d. By treating the capillary walls, prior to the gel synthesis, with HF (48%) the walls were made rough. Indeed, we observed that the wall roughness prevented slippage, Fig. 5.4e-h. Slippage of end 2 was significantly reduced during the shrinking cycle and end 1 almost stayed fixed during the swelling cycle, Fig. 5.4e,f. Furthermore, by using smaller peltier elements (4.2x4.2 mm^2 size versus 9x9 mm^2), the size of the gel segment under stimulus was reduced resulting in reduced slippage due to swelling towards the free surface (end 1) of the first segments of the gel (*slip 2*), Fig. 4f,g. The same principle applied for the shrinking cycle, where the last segment moved backwards while shrinking (*Slip 1*). By making the size of the segment under stimuli smaller we were able to reduce the slippage related to the motion towards the free surface while swelling and shrinking. The slippage factor reduced to 0.19 with these changes in the surface roughness of the capillary walls and the size of the peltier elements, Fig. 5.4h. To summarize, during the shrinking cycle, end 1 moved forward and end 2 stayed fixed throughout and during the swelling cycle, end 2 moved in forward direction while end 1 moved only slightly backwards due to the swelling towards the free

surface, see supporting information. Reducing the slippage improves the device performance with fewer cycles required to move the gel over a given distance.

Conclusions

Our prototype device based on a thermo-responsive organic-inorganic hybrid hydrogel, reproducibly imitates locomotion shown by an earthworm, over many cycles. This device overcomes the shortcomings of our previous pNIPA gel based device which had poor mechanical properties, and required long post-synthesis hydrolysis times to enable large volume changes upon phase transition. The device demonstrated here exhibits high mechanical robustness of the clay nanoparticles-pNIPA nanocomposite gels and requires no hydrolysis time to observe large volume changes. It also demonstrates faster swelling kinetics as a result of introducing heterogeneities in the polymer network by synthesizing the gels at a temperature above their LCST. Additionally, the slippage in the motion of the gels was significantly reduced by making the walls of the capillary rough by HF etching, and by using smaller peltier elements to stimulate shrinking and swelling.

The device we have shown here thus demonstrates reliability, robustness, and fast kinetics, essential characteristics for a microfluidics based device. It thus holds greater promise for future miniaturization experiments than our previous device. We anticipate that the principle described herein will be widely utilized in a variety of areas in biotechnology, microfluidics, small-scale robotics and drug delivery.

Acknowledgments

We would like to thank NSF (DMR-0404195) for financial support through the NIRT program and the Cornell Center for Materials Research (CCMR), with funding from the Materials Research Science and Engineering Center program of NSF (cooperative

agreement DMR-0520404), for the use of facilities. We would also like to thank Andrew Burns for help with the schematic and Hanying Li for discussion about the freeze-drying of gel samples for SEM imaging.

APPENDIX D

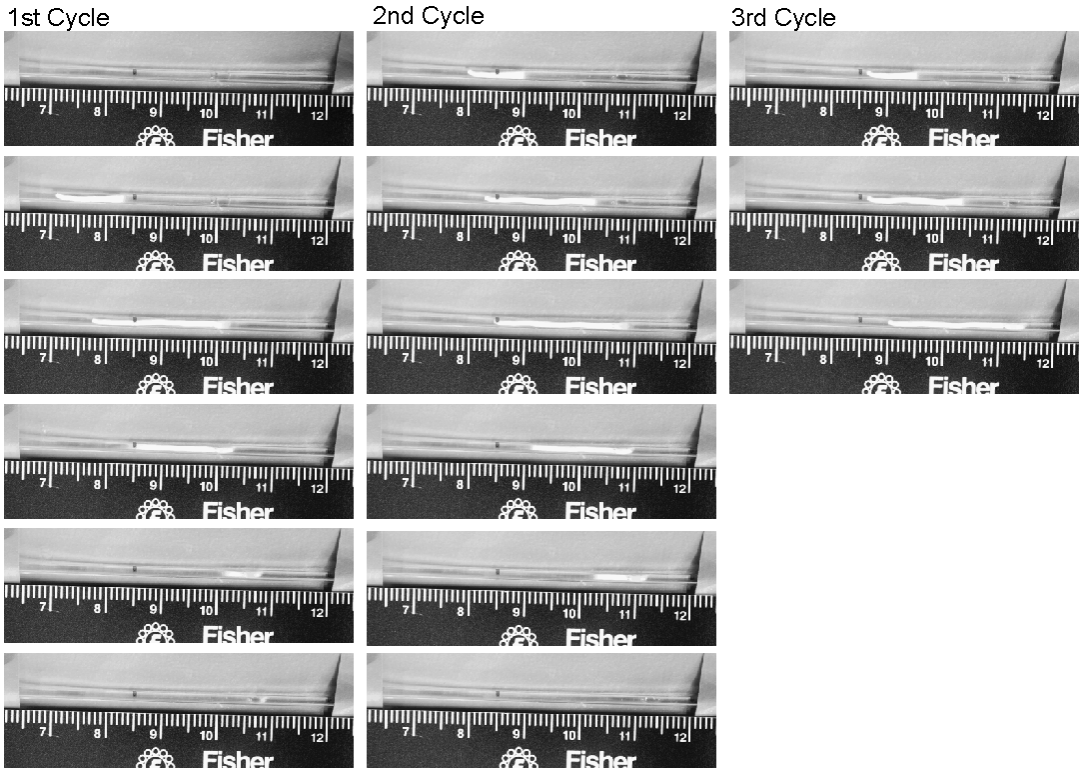

Supporting information: Snapshots taken over 2 hours and 15 minutes, during the fast hybrid gel motion over 3 shrinking and 2 swelling cycles.

REFERENCES

1. Vale, R. D.; Reese, T. S.; Sheetz, M. P., Identification of a novel force-generating protein, kinesin, involved in microtubule-based motility. *Cell* **1985,** 42, (1), 39-50.

2. Schnitzer, M. J.; Block, S. M., Kinesin hydrolyses one ATP per 8-nm step. *Nature* **1997,** 388, (6640), 386.

3. van den Heuvel, M. G. L.; de Graaff, M. P.; Dekker, C., Molecular Sorting by Electrical Steering of Microtubules in Kinesin-Coated Channels. *Science* **2006,** 312, (5775), 910-914.

4. Hutchins, Benjamin M.; Platt, M.; Hancock, William O.; Williams, M. E., Directing Transport of $CoFe_2O_4$-Functionalized Microtubules with Magnetic Fields13. *Small* **2007,** 3, (1), 126-131.

5. Ludk Toman, M. J., Jií Spváek, Jií Brus, Antonín Sikora, Jií Horský, Petr Vlek, Petra Látalová, Amphiphilic conetworks. IV. Poly(methacrylic acid)-l-polyisobutylene and poly(acrylic acid)-l-polyisobutylene based hydrogels prepared by two-step polymer procedure. New pH responsive conetworks. *Journal of Polymer Science Part A: Polymer Chemistry* **2009,** 47, (5), 1284-1291.

6. Tanaka, T.; Fillmore, D.; Sun, S.-T.; Nishio, I.; Swislow, G.; Shah, A., Phase Transitions in Ionic Gels. *Physical Review Letters* **1980,** 45, (20), 1636.

7. Xiao-Ding Xu, C.-S. C., Zong-Chun Wang, Gan-Rui Wang, Si-Xue Cheng, Xian-Zheng Zhang, Ren-Xi Zhuo, Click chemistry for in situ formation of thermoresponsive P(NIPAAm-co-HEMA)-based hydrogels. *Journal of Polymer Science Part A: Polymer Chemistry* **2008,** 46, (15), 5263-5277.

8. Hirokawa, Y.; Tanaka, T., Volume phase transition in a nonionic gel. *The Journal of Chemical Physics* **1984,** 81, (12), 6379-6380.

9. Tanaka, T.; Nishio, I.; Sun, S.-T.; Ueno-Nishio, S., Collapse of Gels in an Electric Field. *Science* **1982,** 218, (4571), 467-469.

10. Suzuki, A.; Tanaka, T., Phase transition in polymer gels induced by visible light. *Nature* **1990,** 346, (6282), 345-347.

11. Yu, L.; Ding, J., Injectable hydrogels as unique biomedical materials. *Chemical Society Reviews* **2008,** 37, (8), 1473-1481.

12. Peppas, N. A.; Hilt, J. Z.; Khademhosseini, A.; Langer, R., Hydrogels in Biology and Medicine: From Molecular Principles to Bionanotechnology. *Advanced Material* **2006,** 18, (11), 1345-1360.

13. Beebe, D. J.; Moore, J. S.; Bauer, J. M.; Yu, Q.; Liu, R. H.; Devadoss, C.; Jo, B.-H., Functional hydrogel structures for autonomous flow control inside microfluidic channels. *Nature* **2000,** 404, (6778), 588-590.

14. Liu, R. H.; Qing, Y.; Beebe, D. J., Fabrication and characterization of hydrogel-based microvalves. *Journal of Microelectromechanical Systems* **2002,** 11, (1), 45-53.

15. Yeghiazarian, L.; Mahajan, S.; Montemagno, C.; Cohen, C.; Wiesner, U., Directed Motion and Cargo Transport Through Propagation of Polymer-Gel Volume Phase Transitions. *Advanced Material* **2005,** 17, (15), 1869-1873.

16. Osada, Y.; Okuzaki, H.; Hori, H., A polymer gel with electrically driven motility. *Nature* **1992,** 355, (6357), 242-244.

17. Mahadevan, L.; S, D.; M, K. C., Biomimetic ratcheting motion of a soft, slender, sessile gel. *Proceedings of the National Academy of Sciences of the United States of America* **2004,** 101, (1), 23-26.

18. Maeda, S.; Hara, Y.; Sakai, T.; Yoshida, R.; Hashimoto, S., Self-Walking Gel. *Advanced Material* **2007,** 19, (21), 3480-3484.

19. Yeghiazarian, L.; Arora, H.; Nistor, V.; Montemagno, C.; Wiesner, U., Teaching hydrogels how to move like an earthworm. *Soft Matter* **2007,** 3, (8), 939-944.

20. Haraguchi, K.; Li, H. J.; Matsuda, K.; Takehisa, T.; Elliott, E., Mechanism of Forming Organic/Inorganic Network Structures during In-situ Free-Radical Polymerization in PNIPA-Clay Nanocomposite Hydrogels. *Macromolecules* **2005,** 38, (8), 3482-3490.

21. Haraguchi, K.; Taniguchi, S.; Takehisa, T., Reversible Force Generation in a Temperature-Responsive Nanocomposite Hydrogel Consisting of Poly(N-isopropylacrylamide) and Clay. *ChemPhysChem* **2005,** 6, (2), 238-241.

22. Andersson, M.; Axelsson, A.; Zacchi, G., Swelling kinetics of poly(N-isopropylacrylamide) gel. *Journal of Controlled Release* **1998,** 50, (1-3), 273-281.

23. Sato Matsuo, E.; Tanaka, T., Kinetics of discontinuous volume-phase transition of gels. *Journal of Chemical Physics* **1988,** 89, (3), 1695.

24. Okano, T.; Bae, Y. H.; Jacobs, H.; Kim, S. W., Thermally on-off switching polymers for drug permeation and release. *Journal of Controlled Release* **1990,** 11, (1-3), 255-265.

25. Zhang, X.-Z.; Xu, X.-D.; Cheng, S.-X.; Zhuo, R.-X., Strategies to improve the response rate of thermosensitive PNIPAAm hydrogels. *Soft Matter* **2008,** 4, (3), 385-391.

26. Yan, Q.; Hoffman, A. S., Synthesis of macroporous hydrogels with rapid swelling and deswelling properties for delivery of macromolecules. *Polymer* **1995,** 36, (4), 887-889.

27. Takata, S.-i.; Suzuki, K.; Norisuye, T.; Shibayama, M., Dependence of shrinking kinetics of poly(N-isopropylacrylamide) gels on preparation temperature. *Polymer* **2002,** 43, (10), 3101-3107.

CHAPTER 6

CONCLUSIONS

In this dissertation, formation, processing, characterization and applications of two different polymer-inorganic hybrid materials were discussed. In the first system, block copolymer self assembly was used to structure direct inorganic nanoparticles (sol-gel derived aluminosilicate and ligand stabilized platinum nanoparticles) to generate hybrid thin films. Subsequently, the organic component was removed to leave behind porous inorganic thin films. The porous thin films were quantitatively analyzed to determine the order in the films. The porous aluminosilicate films were used to generate single crystal nanostructured arrays using pulsed excimer laser induced melting. Furthermore, the pores in the template were used to grow nickel silicide pillars heteroepitaxially on silicon. The growth of the crystal over the template allowed forming a relaxed NiSi lattice. The symmetry of the orthorhombic crystal induced relaxation of NiSi film into two orthogonal (90°) orientations.

In the second system, volume phase transitions of nanocomposite (hybrid) hydrogels were used to generate locomotion of hydrogels inside glass capillaries. Hybrid hydrogels with thermoresponsive polymer chains cross-linked through clay nanoparticles and volume phase transitions at 32 °C were synthesized inside capillaries. Volume changes were induced locally using peltier elements. The volume phase transition was then propagated through the length of the gel, breaking the symmetry and inducing directional motion. The mechanism of locomotion was similar to that shown by an earthworm. Synthesizing the gels above the phase transition temperature resulted in super-porous gels that showed faster swelling kinetics. The capillary walls were roughened to increase the adhesion of the swollen gel on the capillary walls resulting in efficient slip-free gel motion.

Future Work

The length scales accessible through the block copolymer self assembly is controlled though the molecular weight of the block copolymer. Characteristic pore spacing in thin films, 30-40 nm for films used in this dissertation, could be further reduced to generate structures with spacing of 5-10 nm. This would enable fundamental studies such as crystallization within confined pores at these near-atomic length scales. Increasing the aspect ratio of the pores would also enable 3-dimensional analysis, through electron tomography, for elucidation of faceting at the crystalline nanostructure surface.

The process to grow heteroepitaxial crystals on silicon, shown here for orthorhombic NiSi, could also be applied to grow crystals exhibiting cubic symmetry such as germanium. Such a system would have only one relaxed orientation and may enable growing single crystals with few or no defects.

The hydrogel shrinking and swelling kinetics is a diffusion controlled process and scales with the critical dimension of the gel. In the system described in chapter 5, the critical dimension is the diameter of the gel. Through scaling down of the gel diameter, it may be possible to study the scaling relation and its possible breakdown as surface forces are expected dominate at small dimensions and strong adhesion to the walls will limit the gel motion.